Sensitivity of multiangle imaging to natural mixtures of aerosols over ocean

Ralph Kahn, Pranab Banerjee, and Duncan McDonald

Jet Propulsion Laboratory, California Institute of Technology, Pasadena

Abstract. Multiangle remote sensing data can discriminate among aerosol air mass types, as represented by climatologically probable, external mixtures of component particles. Retrievals are performed over a comparison space of four-component mixtures, selected from six commonly observed components having assumed, fixed microphysical properties but with mixing ratios free to vary from 0% to 100%. We refer to this approach, which assumes climatologically probable component particles and derives aerosol mixtures from the observations, as a "climatological retrieval." On the basis of simulated Multiangle Imaging Spectroradiometer (MISR) observations over dark water, the retrieval can distinguish mixtures containing large, spherical particles (sea salt), nonspherical particles (accumulation and coarse mode dust), and small, dark particles (black carbon) to within 20% or better of each component's true mixing ratio. This is sufficient to distinguish maritime from continental aerosol air masses. The retrievals, which use all nine MISR angles and the two wavelengths least affected by ocean surface reflectance (672 and 867 nm), are not good at distinguishing medium, spherical, nonabsorbing (sulfate) from medium, spherical, absorbing (carbonaceous) particles. However, the sum is retrieved to within 20% of the true mixing ratio or better. This is significantly more detail about the properties of particle mixtures than has previously been retrieved from satellite data, and in all cases, the derived total column aerosol optical depth remains well constrained, to at least 0.05 or 20%, whichever is larger. We expect the MISR data, with its frequent global coverage, to complement in situ and field data, which can provide greater detail about aerosol size and composition locally. This combined effort should advance our knowledge of aerosol behavior globally and our ability to model the impact of aerosols on the climatically important solar radiation budget.

1. Introduction

Recent advances in modeling the Earth's climate and studying its radiation balance have brought us to a point where the contributions made by aerosols to the global radiation budget significantly affect the results [e.g., *Andreae*, 1995; *Charlson et al.*, 1992; *Cusack et al.*, 1998; *Hansen et al.*, 1997; *Haywood et al.*, 1999; *Li et al.*, 1997; *Penner et al.*, 1994]. Aerosols are thought to contribute to direct radiative forcing in the atmosphere and indirectly through their influence as nucleation sites for cloud particles. Knowledge of both aerosol optical depth and microphysical properties of particles are needed to adequately model aerosol effects on climate.

Currently, we must rely on satellite remote sensing to provide the spatial and temporal coverage required for global monitoring of atmospheric aerosols. However, the retrieval of aerosol properties by remote sensing is a notoriously underdetermined problem, and the only operational, global-scale, satellite-based retrieval of aerosols derives aerosol optical depth from single-angle, monospectral data, using assumed values for all the aerosol microphysical properties [*Rao et al.*, 1989; *Stowe et al.*, 1997].

Multiangle, multispectral remote sensing observations, such as those anticipated from the Earth Observing System (EOS) Multiangle Imaging Spectroradiometer (MISR), provide a

type of information about the characteristics of aerosols never before obtained from satellites [*Martonchik et al.*, 1998; *Diner et al.*, 1998a]. The instrument is unique in having higher spatial resolution, a wider range of downtrack view angles, and higher precision onboard calibration than even the recently flown POLDER instrument [*Deschamps et al.*, 1994]. MISR was launched into polar orbit on December 18, 1999, aboard the EOS Terra satellite. It measures the upwelling shortwave radiance from Earth in four spectral bands, centered at 446, 558, 672, and 867 nm, at each of nine view angles spread out in the forward and aft directions along the flight path at 70.5°, 60.0°, 45.6°, 26.1°, and nadir. Over a period of 7 min, as the spacecraft flies overhead, a 360 km wide swath of Earth is successively viewed by each of the cameras. As a result, MISR samples a very large range of scattering angles, between about 60° and 160° at midlatitudes. The maximum spatial sampling rate is 275 m, and global coverage is acquired about once in nine days at the equator. The nominal mission lifetime is 6 years.

MISR data are being used to characterize surface albedo and bidirectional reflectance, and cloud properties. We also have algorithms to retrieve aerosol optical depth and to distinguish air masses containing different mixes of atmospheric aerosols, globally.

This is the third in a series of theoretical papers that explore our ability to retrieve information about atmospheric particles from MISR. The first two papers ask how well we can distinguish among particles having systematically and independently varying ranges of microphysical properties. A four-dimensional

space was explored, covering natural ranges of effective size, real and imaginary refractive indexes, and optical depth [*Kahn et al.*, 1998]. A separate investigation looked at optical depth, effective size, and spherical versus randomly oriented nonspherical shapes, for Saharan dust-like composition [*Kahn et al.*, 1997]. The "generic" approach to aerosol retrieval, adopted in these studies, interprets top-of-atmosphere radiances in terms of a column-averaged, cross-section-weighted mean effective aerosol population having unimodal, lognormal size distribution, and uniform composition.

On the basis of the simulations, we showed that over calm ocean surfaces, and with commonly observed ranges of particle optical depth and size distribution, the MISR algorithm can retrieve column optical depth for all but the darkest particles to an accuracy better than 0.05 or 20%, whichever is larger, even if the microphysical properties of the particles are poorly known. It can distinguish spherical from nonspherical particles having Saharan dust-like composition. At most latitudes, MISR can also identify three to four distinct size groups between 0.1 and 2.0 μm characteristic radius and two to three compositional groups over the natural range of refractive indices.

These results indicate that the MISR aerosol retrieval can distinguish about a dozen groupings of particles over the natural range of physical properties: three sizes, two or three compositions, and spherical versus randomly oriented nonspherical particles. This represents a major improvement over current operational remote sensing aerosol retrievals, suggesting that with MISR data, we should be able to track air masses on a global scale based on the microphysical properties of the aerosols within them.

The generic retrieval produces aerosol physical properties with a minimum of assumptions; of the column-average particle microphysical properties, only a distribution function for particle size, though not the characteristic radius itself, is assumed. This is a good approach for assessing the information content of observations. However, the effective column-average particle properties obtained may not correspond to any particles actually observed in the field or predicted by transport models. Under natural conditions, component particles are mixed. Constraints on mixtures of particles in the air mass are needed to (1) identify air mass source regions, (2) track the evolution of air masses as they are advected downstream from their sources, (3) make meaningful comparisons between MISR retrievals and in situ aerosol samples, and (4) make meaningful comparisons between MISR retrievals and transport model results.

In this paper we develop a MISR algorithm for retrieving aerosol air mass types, as represented by external mixtures of component particles. Since it is impractical to test every conceivable mixture of every possible component, we adopt a "climatological" retrieval approach, which asks how well we can distinguish among mixtures of assumed, climatologically probable component particles with MISR data. The additional assumptions allow us to probe directly the way MISR might identify air masses containing common mixtures of aerosols in Earth's atmosphere and to compare retrieval results with in situ observations and with aerosol transport model predictions.

Some of the best known satellite aerosol retrieval algorithms currently in use are climatological algorithms. These include the advanced very high resolution radiometer (AVHRR) standard retrieval [*Stowe et al.*, 1997], and a two-channel algorithm applied to the Ocean Color Temperature Scanner (OCTS) instrument, which flew aboard the ADEOS spacecraft [*Higu-*

rashi and Nakajima, 1999]. These algorithms adopt one- or two-component climatologies, appropriate to data from the previous generation of remote sensing instruments but not adequate to take advantage of the additional information about particle properties in the MISR multiangle observations.

In section 2 we develop a climatology of four-component mixtures, based on an analysis of published global, monthly aerosol transport model results. This climatology is rich enough to represent a range of aerosol characteristics covering the entire transport model data set, to at least the level of detail to which MISR is sensitive, based on the generic retrieval results. We also make an effort to assess the quality of the climatology data, since the value of a climatological retrieval rests on the accuracy of the assumed climatology. Section 3 describes the way we analyze the multidimensional particle mixture sensitivity data. As in previous studies, we concentrate on situations under which the MISR sensitivity to particle properties (except possibly absorption) is likely to be greatest: over cloud-free, calm ocean. Results and conclusions are presented in the subsequent sections.

2. An Aerosol Climatology of Four-Component Mixtures

One of the motivations for flying MISR and other EOS instruments is that current knowledge of the global-scale distribution of aerosol air mass types is inadequate for the purposes of many climate change studies. However, the slate is not completely blank. Field observers have identified about a half-dozen broad classes of component aerosols (though their detailed properties vary considerably in space and time) and have discovered that only certain combinations of components are found commonly in nature [e.g., *Prospero et al.*, 1983; *d'Almeida et al.*, 1991; *Kopke et al.*, 1997, and references therein]. We use results from a collection of global transport models (summarized by *Tegen et al.* [1997]) to identify climatologically probable groupings of component aerosols.

Each transport model estimates the monthly global distribution of one or more of six common component aerosols: sulfate, carbonaceous, and black carbon particles [*Liousse et al.*, 1996], accumulation and coarse mode dust [*Tegen and Fung*, 1995], and sea-salt particles [*Tegen et al.*, 1997]. Some characteristics of these models are given in Table 1. We resampled each model output to a uniform 1° by 1° global grid, using bilinear interpolation. (At the 1° scale, the model results are smooth, so resampling does not introduce spurious gradients.) For each model, the aerosol column mass per unit area was converted to an optical depth contribution using the factor in column 6 of Table 1. We linearly superposed the six data planes to obtain a global grid containing monthly estimates of total column aerosol optical depth and a fraction of total optical depth contributed by each of the component aerosols, evaluated at midvisible wavelengths (MISR band 2, at 558 nm).

The climatology developed in this section amounts to a new classification of aerosol mixtures. It is aimed at meeting two objectives. First, it must boil the transport model results down to a small number of aerosol component groupings, which we call mixing groups, which encompass the climatologically probable combinations of component aerosols for all locations and months. A mixing group consists of all possible fractional amounts of four component aerosols; the microphysical properties of each component are assumed and fixed, but the mixing ratios of each component are free to vary from 0% to

Table 1. Monthly, Global Aerosol Transport Models Used in This Study

Component Aerosol	Source	Reference	Spatial Resolution	Quantities Reported	Units Given	Factor Used to Convert Column Mass per Area to τ
Accumulation and coarse mineral dust*	GISS	*Tegen and Fung* [1995]	4° × 5°	total column dust optical depth, regrouped into 2 size bins: <1 μm (accumulation), 1–10 μm (coarse)	none	1.5 m² g⁻¹ (accumulation mode); 0.3 × m² g⁻¹ (coarse mode)
Sea salt*	GISS	*Tegen et al.* [1997]	4° × 5°	total column aerosol optical thickness	none	0.3 m² g⁻¹
Sulfates†	LLNL	*Liousse et al.* [1996]	~4.5° × 7.5°	column mass load	g m⁻²	8.5 m² g⁻¹
Carbonaceous particles*	GISS	*Liousse et al.* [1996]	4° × 5°	total column aerosol optical thickness	none	8.0 m² g⁻¹
Black carbon*	GISS	*Liousse et al.* [1996]	4° × 5°	total column aerosol optical thickness	none	9. m² g⁻¹
Total aerosol‡ (assumes "sulfate" optical properties)	NOAA/AVHRR	*Stowe et al.* [1997]	1° × 1° global oceans +70° to −70° latitude	total column optical depth (at 0.63 μm)	none	optical depth adjustment applied $\tau' = 1.56\tau + 0.03$
Sulfates*	GISS	*Chin et al.* [1996]	4° × 5°	total column aerosol optical thickness	none	6.0 m² g⁻¹ (land); 10 m² g⁻¹ (ocean)

*Data obtained from *Tegen et al.* [1997], Goddard Institute of Space Studies (web site (http://www.giss.nasa.gov/gacp/transport/) 1997.
†Obtained from J. Penner et al., from the Lawrence Livermore National Laboratory (LLNL) model, personal communication, 1998.
‡Obtained from L. Stowe et al., National Oceanographic and Atmospheric Administration (NOAA), personal communication, 1997.

100%, in increments of 5%. This produces 1771 mixtures per mixing group. We find that five mixing groups are needed to span the climatology. In subsequent sections we test each set of measurements by comparing it with all mixtures in all five mixing groups, for each of 21 values of column aerosol optical depth, a total of 185,955 comparison models.

The second goal of the climatology is to identify air mass types, composed of specific fractional amounts of component particles in the mixing groups, which give a fair representation of the global-scale spatial and temporal aerosol mixture patterns. These representative air mass types are not needed for climatological retrievals with MISR data, but for the sensitivity study, they are used to generate sample measurements. The sensitivity study asks how narrow a range of mixtures, from among all those in the entire comparison space, give acceptable matches to the simulated MISR radiances in each set of sample measurements. A narrower range indicates that the retrieval is more specific as to the identity and fraction of each component present.

2.1. Mixture Classification

We begin by defining mixing groups as combinations of component particles in the aerosol climatology. We expect MISR to make about a dozen distinctions based on aerosol microphysical properties [*Kahn et al.*, 1998, 1997]. This amount of detail is captured by mixtures of four component aerosols; having fewer components would eliminate some climatologically common mixtures that MISR can identify, whereas including more components adds only redundant retrieval results. So we classify the six-layer, aggregated, global transport model data set according to the four component particles that contribute most to the total column optical depth at each location and month. The two components that contribute least to a given space-time grid cell are ignored for that cell.

Plates 1a–1d give maps of particle mixing groups for 4 months spanning the year. The corresponding total column optical depths, also derived from the aggregated transport model results, are shown in Plates 2a–2d. Although the model results for most aerosol components were developed independently of each other, the mixture data are highly clustered. Of the 15 possible combinations of four component particles that can be made from the six included in the climatology, only five combinations are needed to describe the top four components for nearly the entire data set. This is an enormous simplification, indicating that in at least one respect, the aggregated transport models reflect aerosol mixture patterns noted by field observers. These mixing groups meet the first objective of the climatology, to provide a broad comparison space. Their compositions are given as major headings in Table 2.

All five mixing groups contain sulfate particles. We label as "maritime" those groups that contain sea-salt particles; we call "continental" those groups that do not have sea salt among the four most abundant component particles but do have accumulation mode dust. The other aerosol components contributing to each group determine whether the classification is "dusty," "carbonaceous," or "black carbon." Representative colors for the maps in Plate 1 are chosen so that the most common maritime classes appear in shades of blue; the most common continental classes are brown. For those that remain, classes rich in black carbon are gray, those having high carbonaceous aerosol fraction are green, and the ones abundant in coarse dust are yellow.

We now address the second objective of the climatology, to

Table 2. Climatological Mixing Groups and Representative Air Mass Types

Classification	Component 1	Component 2	Component 3	Component 4	Notes
1. Carbonaceous + dusty maritime	sulfate	sea salt	carbonaceous	accum. dust	34% of voxels are nonzero
1a	(0.67)	0.13	0.10	0.10	middle- to high-latitude oceans, winter; Nov.–May, southern oceans; May–Sept., North Atlantic
1b	0.41	0.13	(0.27)	(0.19)	tropical to subtropical oceans, all year; June–Oct., remote southern oceans
1c	0.40	(0.32)	0.17	0.11	southern midlatitude oceans, all year; Nov.–March, remote southern oceans
2. Dusty maritime + coarse dust	sulfate	sea salt	accum. dust	coarse dust	14% of voxels are nonzero
2a	(0.52)	0.17	0.21	0.10	downwind of deserts: Australia, Africa, South America, peak during southern summer; Oct.–Jan., N. W. Africa
2b	0.29	0.13	(0.39)	(0.19)	same pattern as 2a but closer to continental source regions
3. Carbonaceous + black carbon maritime	sulfate	sea salt	carbonaceous	black carbon	11% of voxels are nonzero
3a	(0.51)	0.18	0.26	0.05	ocean near Indonesia, all year; Dec.–March, North Atlantic; Jan.–Feb., oceans near central Africa; May–July, oceans near tropical South America; July–Sept., oceans near central America
3b	0.35	0.10	(0.47)	(0.08)	same pattern as 3a but closer to continental source regions
4. Carbonaceous + dusty continental	sulfate	accum. dust	coarse dust	carbonaceous	21% of voxels are nonzero
4a	(0.61)	0.21	0.05	0.13	Feb.–Nov., eastern North America; July–Sept., western North America; Jan.–March, South America; Jan.–March, southern Africa; Oct., India; July–Oct., Korea
4b	0.40	(0.35)	0.09	(0.16)	March–July, Oct.–Nov., western North America; Sept.–Dec., South America; April–Oct., S. Africa; Jan.–March, central Asia; April–June, Nov.–Dec., Korea
4c	0.22	(0.51)	(0.16)	0.11	Arabia and North Africa, all year; Nov.–Dec., S. Africa; March–Dec., central Asia; Jan.–April, July–Dec., Australia
5. Carbonaceous + black carbon continental	sulfate	accum. dust	carbonaceous	black carbon	15% of voxels are nonzero
5a	(0.59)	0.12	0.23	0.06	April–Oct., Europe; Jan.–March, north Asia; July–Sept., east China; Nov.–March, east North America; Nov.–March, equatorial South America
5b	0.25	0.12	(0.54)	0.09	Tropical-subtropical Africa, all year; Dec.–March, west Europe; Jan.–March, north Asia; Jan.–March, east China
5c	0.44	(0.23)	(0.26)	0.07	Nov.–Jan., west Europe; Oct.–March, east Europe; Nov.–Feb., north Asia; Oct.–Dec., April–July, east China; Dec.–April, equatorial South America

Relative abundances are given as fractions of the total optical depth in MISR band 2 (558 nm effective wavelength). Numbers in parentheses are distinctive constituents of the mixture. "Accum. dust" stands for accumulation mode dust.

identify representative air mass types having specific fractional amounts of component particles, to be used as sample atmospheres in the sensitivity study. Plate 3 illustrates that the actual proportions of the four components within each group are also highly clustered in the transport model results. This plate shows slices through a four-dimensional histogram of the aerosol components for the "carbonaceous + dusty continental" mixing group, aggregated over the year. The full diagram is a tetrahedron, divided into voxels that correspond to mixtures having different proportions of each of the four component particles (in this case: sulfate, accumulation mode dust, coarse mode dust, and carbonaceous particles). Vertices of the tetrahedron represent 100% of a component, and along the edges are mixtures of only two components. Each triangular facet is a standard ternary mixing diagram; in the facet interior are three-component mixtures of systematically varying proportions. Points interior to the tetrahedron volume correspond to four-component mixtures. For this four-dimensional histogram we have chosen a 5% increment. The voxel at one of the vertices of the tetrahedron is colored according to the number of occurrences in the climatology of a mixture with 100% of the component aerosol associated with that vertex, immediately adjacent voxels have at least 95% but less than 100% of that component, etc.

Plate 3 shows six planes having constant coarse mode dust fraction, corresponding to bins containing coarse mode dust of

(1) 25–30%, (2) 20–25%, (3) 15–20%, (4) 10–15%, (5) 5–10%, and (6) 0–5%. Red shades indicate high counts (>2500), gray are intermediate values (about 1200–2500), light blue are values between 600 and 1200, dark blue are counts below 600, and black are locations for which there were no mixtures in the climatology falling in that mixture bin. The maximum value is a bright red voxel in panel (5) with 5895 counts and an average mixture of 47% sulfate, 13% carbonaceous, 33% accumulation mode dust, and 7% coarse mode dust (percent by optical depth). In the computer-interactive tool we can select four-dimensional histograms for any mixing group, aggregated either by month or for the full year. We can view planes having constant fraction of any component and select individual voxels in the planar representations to bring up the number of counts and mean proportions of each component contributing to that voxel.

Of 1771 voxels in this histogram, only 21% are nonzero. For this mixing group, planes for which the coarse mode dust component is greater than 40% are all empty. The voxels having nonzero counts are concentrated in a small part of the volume, and there are several local maxima, some of which show up better in the monthly histograms than in the annual aggregate. The other four mixing groups behave similarly and contain between 11 and 34% nonzero voxels (Table 2), all concentrated in two or three clusters. This clustering represents a further simplification in the climatology and is another way the aggregated transport models reflect patterns seen by field observers.

We used a K-means clustering algorithm [*Hartigan and Wong*, 1979] to locate the centroids of clusters in each mixing group. Given a number (K) of clusters to be identified, the alogrithm locates cluster centers that minimize the sum (over all points) of the squared distance from each point in the space to its nearest cluster center. We use the percent contributions to total column optical depth of the four components as four linear metrics spanning the space. K-means algorithms depend heavily on the choice of K and also on initial guesses for the cluster center locations. We used the interactive, computer-based four-dimensional histogram tool (Plate 3) to identify initial guesses. We also experimented with the number and order of initialization values to assure that we found stable solutions and reviewed the monthly histograms and maps to search for clusters that may not show up well in the annual aggregates. The resulting 13 cluster centroids, given in Table 2, are the representative aerosol air mass types we use for the sensitivity study. The spatial distributions of the mixing groups, subdivided into the 13 air mass types, are shown for 4 months spanning the year in Plates 1e–1h. Some attributes of air mass type spatial and temporal behavior are also summarized in Table 2, column 6.

2.2. Assessment of the Climatology

Since the value of the climatological retrieval rests on the quality of the assumed climatology, we made an effort to understand its strengths and limitations. In qualitative terms, the patterns created by our classification scheme compare favorably with expectation and with observations [*Tegen et al.*, 1997, and references therein; see also *Husar et al.*, 1997]. Continental classes predominate over most land masses and downwind in some coastal regions; maritime classes are found away from continents. Black carbon classes appear over Europe, eastern China, and tropical Africa and South America. Carbonaceous classes occur in the equatorial zone, persistently over Indone-

sia. Coarse dust is a major component over deserts and surrounding areas. Over oceans, at places more distant from the terrestrial sources of dust, biomass burning, or soot, the air masses tend to contain larger fractions of sulfates and sea-salt particles.

The classification is less meaningful where optical depth is low, since tiny amounts of one component can determine the class. This occurs in the polar regions, remote oceans, and high-latitude continental areas, particularly in winter. More generally, the climatology's optical depths, illustrated in Plates 2a–2d, also match qualitative, global-scale expectations: they are highest over well-known source regions such as the Sahara and Gobi deserts, the tropical rainforests and subtropical savannas during burning seasons, and major industrial areas such as eastern Europe and eastern China. Total column optical depths are also higher in summer than in winter in each hemisphere, and seasonal effects are greater in the land-rich Northern Hemisphere.

Our evaluation must take into account uncertainties in the transport models themselves, such as the assumption, for each component aerosol, of a universal value for the factor that converts column mass abundance to optical depth (Table 1). Due, in part, to the choices made for these factors, maritime classes appear over western North America and parts of South America and subtropical Africa between January and April. Carbonaceous particles appear among the top four components at almost all locations and times. As discussed by *Tegen et al.* [1997], there are other limitations to the transport model results, caused by model error, simplified parameterizations of physical processes, and unmodeled aspects of natural variability.

We take a few steps in the direction of a more quantitative, global assessment of the climatology, by comparing the model optical depth results with monthly aerosol optical depth retrievals over global oceans from the NOAA AVHRR measurements [*Stowe et al.*, 1997; *Rao et al.*, 1989] (Table 1). The AVHRR retrieval is not specific as to component particle properties. Aerosol indices of refraction are assumed to be globally constant and equal to $1.4 - 0.0i$. Particles are taken to have a lognormal size distribution with characteristic radius of 0.1 μm and distribution width 2.03. The ocean surface is assumed to have a reflectivity of 0.002 at 0.63 μm. Retrievals are performed only over cloud-free ocean, between 70° north and 70° south latitudes.

Global maps of the difference in total column aerosol optical depth between the AVHRR and the transport model results, for 4 months in 1989, a year without major volcanic contributions to the global aerosol load, are shown in Plates 2e–2h. The comparison must be viewed with caution: the AVHRR data are skewed toward cloud-free regions, which may produce an underestimate of aerosol optical depths on regional scales [*Tegen et al.*, 1997]; they are not sensitive to contributions from absorbing particles, and a single component aerosol is assumed. Nevertheless, the AVHRR data often report larger column optical depths than the aggregate of aerosol transport models; histograms of monthly global optical depth difference for 1° by 1° spatial cells (not shown) are skewed by about 0.05 in the direction of higher AVHRR values.

The AVHRR optical depth values range from the limit of detection up to about 1.0 and are generally within 0.2 of the model predictions. On a global scale, the biggest discrepancies between AVHRR and the models occur in the corridor where Saharan dust is advected westward across the Atlantic and in the Arabian Sea. Optical depths are relatively high in these

Table 3. Component Aerosol Properties Assumed for Climatology*

Component Aerosol	r_1, μm	r_2, μm	r_c, μm	σ	n_r, MISR Band	n_i, MISR Band	ω_0, 672 nm	RH, %	Particle Size/ Shape Category
Sulfate (accum.) over land	(0.007) 0.007	(0.7) 0.81	(0.07) 0.08	(1.86) 1.88	(1.53) 1.46	0.0 (all)	1.0	(0) 70	medium spherical
Sulfate (accum.) over ocean	(0.007) 0.008	(0.7) 1.05	(0.07) 0.10	(1.86) 1.87	(1.53) 1.39	0.0 (all)	1.0	(0) 80	medium spherical
Sea salt (accum.)	(0.05) 0.098	(1.0) 1.98	(0.35) 0.61	(2.51) 2.29	(1.50) 1.35	0.0 (all)	1.0	(0) 80	large spherical
Mineral dust† (accum.)	0.05	2.0	0.47	2.60	1.53	0.0085 (1) 0.0055 (2) 0.0045 (3) 0.0012 (4)	0.91	—	medium nonspherical
Mineral dust† (coarse)	0.5	15.0	1.90	2.60	1.53	0.0085 (1) 0.0055 (2) 0.0045 (3) 0.0012 (4)	0.73	—	large nonspherical
Carbonaceous‡	0.007	2.0	0.13	1.80	1.50	0.025 (all)	0.87	97	medium spherical
Black carbon	0.001	0.5	0.012	2.00	1.75	0.455 (1) 0.440 (2) 0.435 (3) 0.430 (4)	0.17	—	small
Thin cirrus§	3.0	200.	⋯	⋯	1.316 (1) 1.311 (2) 1.308 (3) 1.304 (4)	0.0 (all)	1.0	100	very large fractal

*In this table, r_1 and r_2 are the lower and upper radius limits for the particle size distribution. "Accum." stands for "accumulation mode" particles. Particle types are distributed lognormally, with characteristic radius r_c and width σ; ω_0 is the single-scattering albedo, given here at the effective wavelength of the MISR red channel. RH is the relative humidity to which hygroscopic particles are hydrated. Sulfate and sea-salt particles are hydrated to the RH value in column 9 using the model of *Hanel* [1976]; where properties for these particle types are in parentheses, they refer to the dry particles. The aerosol physical data are abstracted from *Shettle and Fenn* [1979], *d'Almeida et al.* [1991], *WCP* [1984], and other sources, except as indicated. Optical data for spherical particles are calculated using standard Mie theory.

†Nonspherical (randomly oriented mixed spheroid) mineral dust models based on *Mishchenko et al.* [1997].

‡Carbonaceous particle model based on *Reid et al.* [1998].

§Fractal thin cirrus model based on *Mishchenko et al.* [1996].

regions to begin with. The AVHRR values usually exceed those of the model results by 0.25–0.5 over the mid-Atlantic (the extreme discrepancy is 0.8, and occurs in July), whereas the model results are mostly between 0.1 and 0.3 higher than AVHRR in the Arabian Sea, with the largest difference just under 0.5. For the purposes of the MISR sensitivity study, this represents good agreement; it provides climatological ranges of optical depth values upon which to focus the simulations.

To further assess the particle mixture classification part of the climatology, we reclassified the air masses after replacing the sulfate model from *Liousse et al.* [1996] with model results from *Chin et al.*, [1996] (see Table 1). (Only for sulfates were we able to obtain comparable, monthly global transport model results from several sources.) Although this is far from a thorough test, it is a useful step to take for this study, since we are interested in general characteristics rather than details. We view differences between the two classifications as suggestive of the accumulated uncertainties in the climatology as they relate to our classification scheme.

Differences between the two sets of models produce different air mass classifications over Europe, and in some low optical depth regions of the North Atlantic and North Pacific. In particular, where sulfur emissions are high, such as Europe, the *Liousse et al.* [1996] model produces several times the optical depth in sulfate particles compared to *Chin et al.* [1996]. The differences are most pronounced in summer.

However, with these exceptions an instrument sensitive to the differences in aerosol mixtures captured by our classification scheme would identify similar aerosol air mass types everywhere else around the globe, given climatologies based on

either transport model. Despite the qualitative nature of the classification scheme its value for the MISR sensitivity study stems from the agreement with expectation, since we classified the transport model results based only on relative abundances of component particles and not on any externally imposed spatial or temporal constraints. Similarly, we hope to derive rather than assume the spatial and temporal patterns of aerosol air mass types from MISR data.

2.3. Assumed Component Particle Optical Properties

Using the transport model results, we obtained representative mixtures of four components from among six component aerosols, given in fractions of the total column optical depth at midvisible wavelengths, on a monthly, 1° by 1° global grid. We also obtained representative values of total column optical depth on the same grid. To complete the climatology needed to assess MISR sensitivity, we must select optical properties for each of the six component aerosols. This is the most difficult part of the climatology to specify, since aerosol properties vary on many spatial and temporal scales. For example, hygroscopic particle properties change substantially depending on the relative humidity [e.g., *Hegg et al.*, 1993], and mineral dust properties vary with source region [*Sokolik and Toon*, 1996].

Since we expect to distinguish about three size groupings, two shapes, and two or three groupings of single-scattering albedo under good observing conditions with MISR data [*Kahn et al.*, 1998, 1997], we selected just one representative set of properties for each of the six components in this sensitivity study, except sulfates. Our choices for particle properties are given in Table 3. They are abstracted from standard sources, as
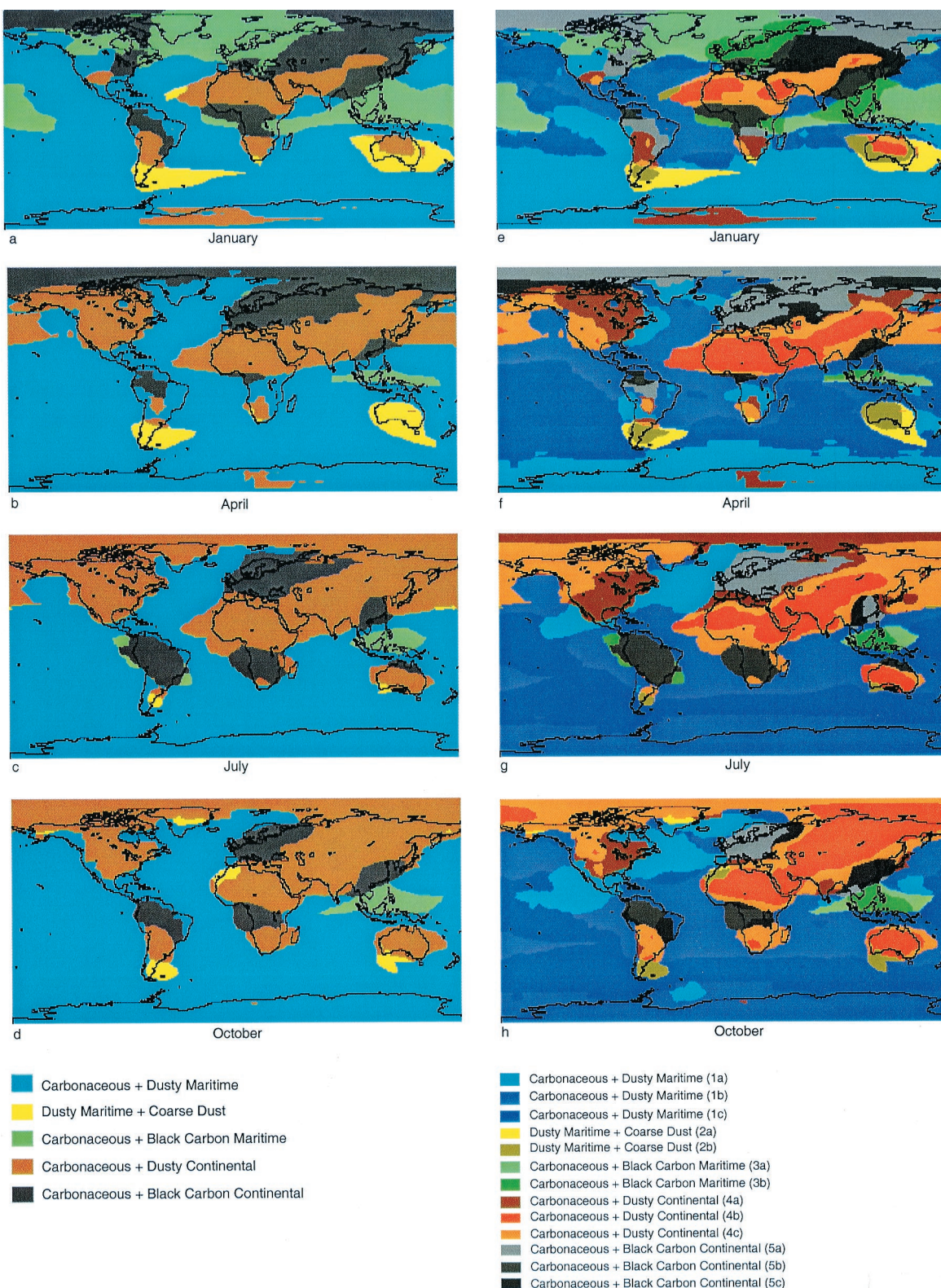
Plate 1. (a–d) Global maps for January, April, July, and October, respectively, showing the spatial distribution of the five aerosol mixing groups defined as major headings in Table 2, based on the aggregate of aerosol transport models listed in Table 1. (e–h) Global maps for January, April, July, and October, respectively, showing the spatial distribution of the 13 representative air mass types, defined in Table 2. To obtain these maps, each point was first classified by aerosol mixing group and then subclassified according to the representative air mass type nearest it, using percent contributions to total column optical depth of each component as the four-dimensional, linear distance metric.
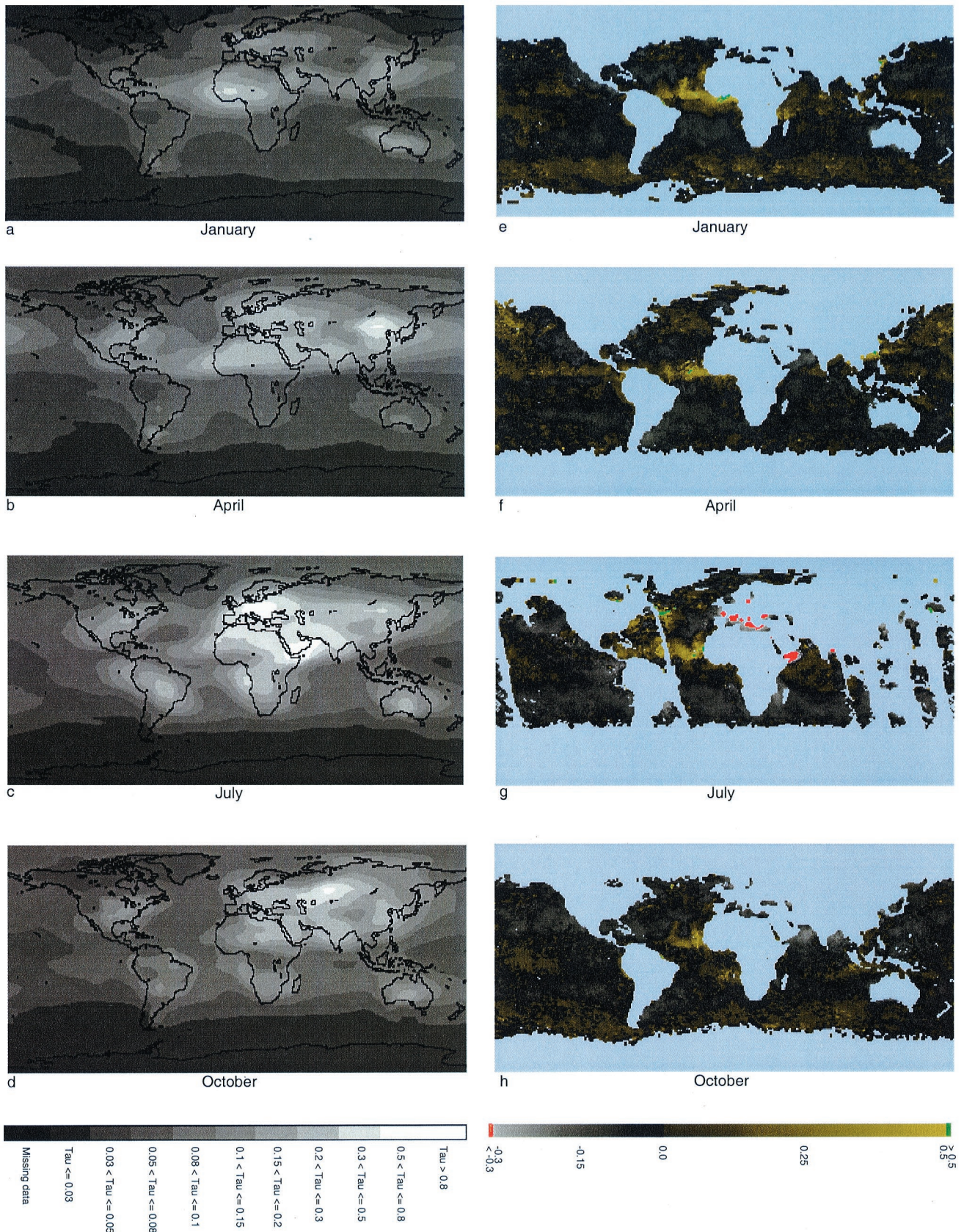
Plate 2. (a–d) Global maps of total column aerosol optical depth ("tau") for January, April, July, and October, respectively, derived from the transport models of *Tegen et al*. [1997]. (e–h) Difference maps between AVHRR-retrieved total column aerosol optical depth for 1989 [*Stowe et al*., 1997] and the corresponding monthly transport model results for January, April, July, and October, respectively. The blue regions indicate places where no AVHRR data exist.
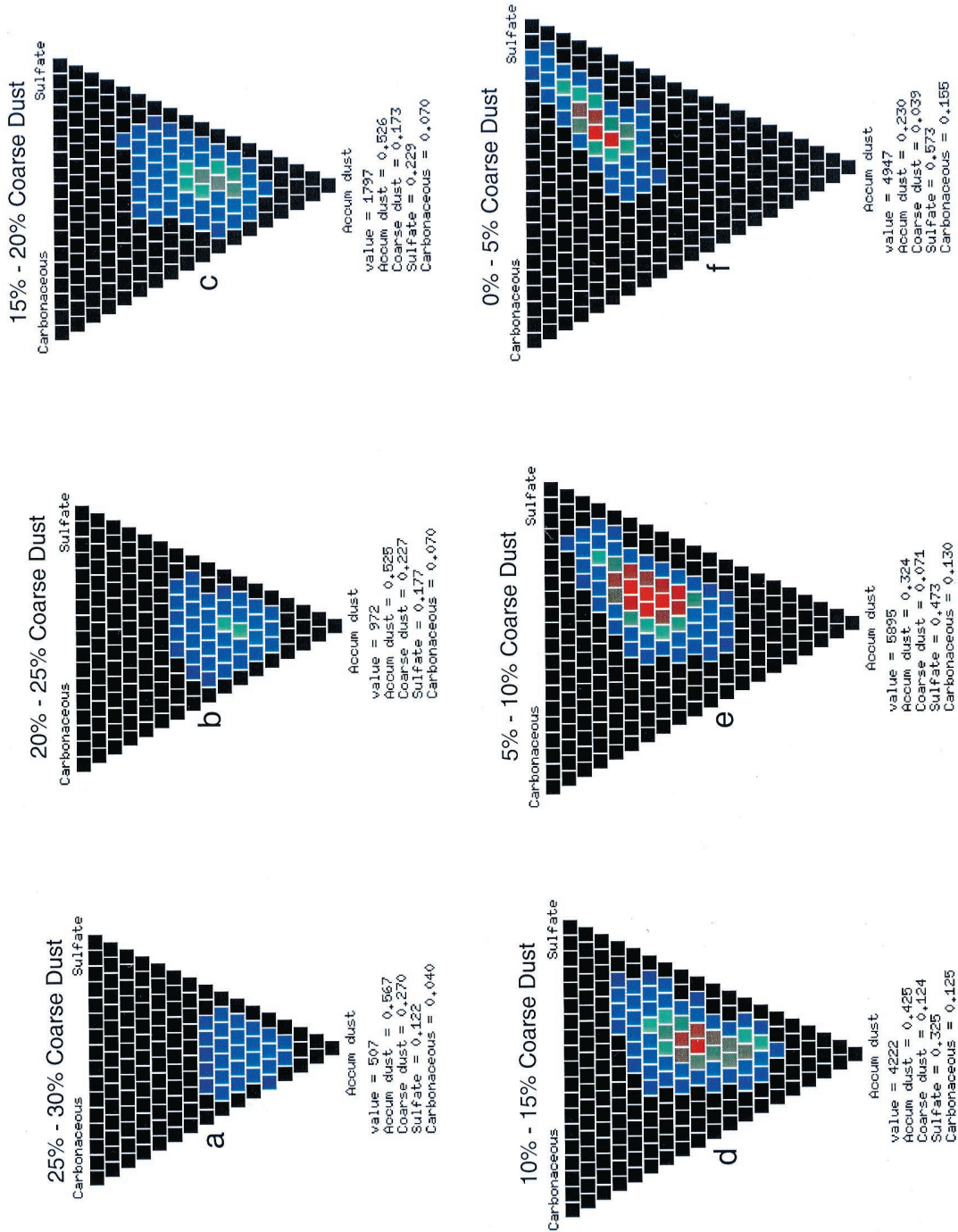
Plate 3. Example of sections through a four-dimensional histogram, showing clustering in the climatological proportions of the aerosol components for mixing group 4 ("carbonaceous + dusty continental" in Table 2), aggregated over a year. This mixing group includes sulfate, accumulation mode dust, coarse mode dust, and carbonaceous particles. Shown here are six planes having constant coarse mode dust fraction, corresponding to bins of (a) 25–30%, (b) 20–25%, (c) 15–20%, (d) 10–15%, (e) 5–10%, and (f) 0–5%. Red shades indicate high counts (>2500), gray are intermediate values (about 1200–2500), light blue values range from 600 to 1200, dark blue are counts below 600, and black are locations for which there were no mixtures in the climatology falling in that mixture bin. Below each section are numerical values of the number of hits, and the average fraction of each component, for the most heavily populated pixel in that section. See text for further details.
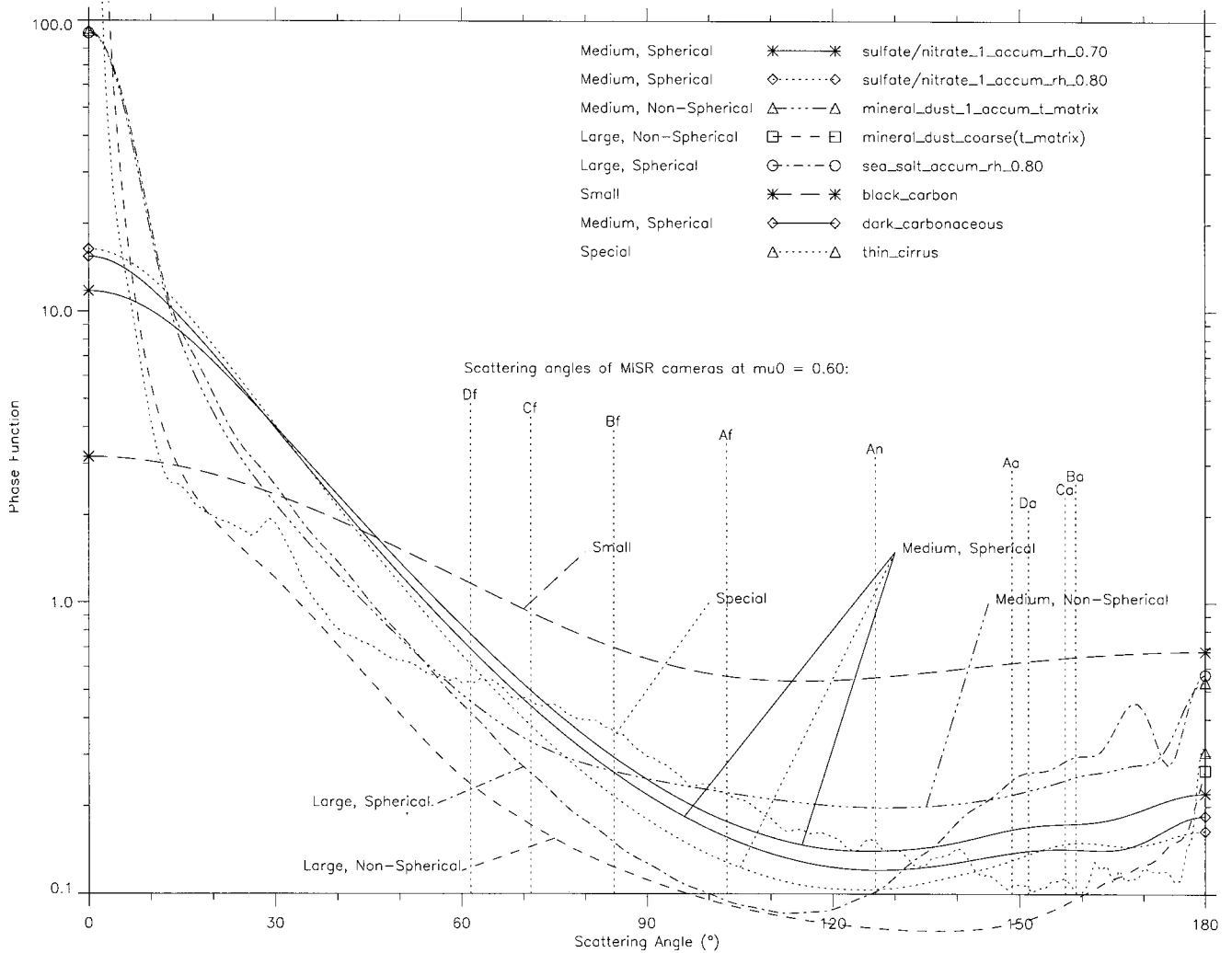
Figure 1. Single-scattering phase functions for six particle types (including two hydration states for sulfate particles) and thin cirrus, for MISR band 3 (672 nm effective wavelength). Detailed physical properties for these particles are given in Table 3. Superposed on this plot are the scattering angles sampled by the nine MISR cameras for a typical midlatitude case. Camera designations are "A," "B," "C," and "D" for the four pairs of cameras viewing at shallow through steep viewing angles, respectively, "f" for forward looking, "a" for aft-looking, and "An" for nadir-viewing cameras.

referenced in this table.

We hydrated the sulfate particles to equilibrium at 70% relative humidity for "continental" air mass types and to 80% for "maritime" air masses using the hydration model of *Hanel* [1976]. We also defined two vertical distributions for accumulation mode dust; one, used for "continental" air mass types, places all the dust in a near-surface layer, as we do for all other components. The second, used for "maritime" air masses to simulate dust particles transported far from their source regions, distributes the particles between 5 and 10 km above the surface, with a scale height of 10 km. We used a Mie algorithm to relate physical to optical properties for the spherical particles; for nonspherical dust and cirrus, we obtained T-matrix results from *Mishchenko et al.* [1996, 1997; personal communication, 2000]. Extinction and scattering properties for distributions of particles are calculated as weighted averages. The lognormal size distribution used is

$$\frac{dN(r)}{dr} = \frac{1}{r \ln (\sigma) \sqrt{2\pi}} \exp \left[- \frac{(\ln (r) - \ln (r_c))^2}{2(\ln (\sigma)^2)} \right]. \quad (1)$$

The width parameter (σ) and characteristic radius (r_c) for each case are given in Table 3, and $N(r)$ is the number density of particles at radius (r).

Of special interest is column 10 in Table 3, which gives a "particle size/shape category" for each entry. These relate to the particle-scattering phase functions shown in Figure 1. Scattering angles imaged by the nine MISR cameras for a typical midlatitude location are superposed in this figure.

The prototypical black carbon particle size distribution produces a characteristic "small particle" scattering phase function. (For small particles, particle shape does not alter the scattering phase function, so the distinction between spherical and nonspherical is moot.) Accumulation mode dust is a medium, nonspherical component, producing a relatively flat scat-

tering phase function between a 70° and 160° scattering angle. Carbonaceous particles, as well as the two sulfate components, are categorized as medium, spherical. The coarse mode dust and sea salt are large, nonspherical and large, spherical particle types, respectively. Each has a steeply sloped scattering phase function at small scattering angles. The thin cirrus model produces a scattering phase function distinct from the other component aerosols. We also expect to distinguish absorbing ("dirty") from nonabsorbing ("clean") particles. In Table 3 the dust, carbonaceous, and black carbon particles are absorbing. It is on the basis of these differences among particle scattering phase functions and absorption characteristics that we expect to discriminate among natural mixtures of particles with MISR data.

3. Our Approach to the Aerosol Mixture Sensitivity Study

Our approach to the climatological sensitivity study is similar to that adopted by *Kahn et al.* [1998] for the generic retrieval study. We use simulations of top-of-atmosphere radiation to explore the sensitivity of multiangle observations to aerosol properties. The MISR Team has developed a radiative transfer code, based on the matrix operator method [*Grant and Hunt*, 1968]. It simulates reflectances as would be observed by MISR for arbitrary choice of aerosol mixture, amount, and vertical distribution, variable surface reflectance properties, and user-selected Sun and viewing geometry [*Diner et al.*, 1998a]. Radiances for mixtures of aerosol components are obtained by combining radiances for the individual components, weighted by their fractional contribution to optical depth, according to the modified linear mixing method of *Abdou et al.* [1997]. For the present study we simulated MISR measurements over a Fresnel-reflecting flat ocean surface, in a cloud-free, Rayleigh-scattering atmosphere with a surface pressure of 1.013 bar, a standard midlatitude temperature profile, and aerosols (except transported accumulation mode dust) concentrated in a near-surface layer.

We assume here that the vertical distribution of aerosols has a negligible effect on the results. Our tests with particles inside and above the Rayleigh scattering layer show that the effect may be significant, particularly at the blue and green wavelengths and at the steepest viewing angles. However, most atmospheric aerosols are concentrated near the surface, and the MISR dark water retrievals use only the red and infrared channels, for which Rayleigh scattering is small. Other particle models will be added as needed when we are analyzing MISR data, particularly when we have the benefit of detailed field measurements at the observation site. For MISR retrievals over ocean we also model Sun glint and whitecaps, which depend on near-surface wind speed [*Martonchik et al.*, 1998], and of course, we anticipate modifying the MISR retrieval algorithm, as needed, as we gain experience working with spacecraft data.

We designate one set of simulated reflectances as the MISR "measurements." For a measurement the atmosphere has a fixed total aerosol optical depth and specified fractional contributions from each of four component particles. We then test whether the measured radiances can be distinguished, within instrument uncertainty, from a series of "comparison" model reflectances. The five mixing groups identified in the climatology and listed as the major headings in Table 2 define the space of comparison models. Each comparison model represents a choice of four component particles. We vary the mixing ratio of each component systematically from 0 to 100%.

Test results for one set of measurements, against all possible comparison models within a mixing group, can be arranged in a tetrahedron, similar to the four-dimensional histograms used for the climatology analysis (Plate 3). The vertices of the tetrahedron represent tests against comparison models containing 100% of each of the four components, the edges are tests against mixtures of two components, the facets show tests against three components arrayed in standard ternary diagrams, and the interior voxels represent tests against four-component mixtures. We use a grid of 5% steps in each dimension.

We also vary the total aerosol optical depth for comparison models over a grid, ranging from 0 to 1 in steps of 0.05. So the entire comparison-model parameter space for a climatological retrieval consists of five mixing groups, each composed of 21 tetrahedra that cover the range of total optical depth values, a total of nearly 186,000 comparison models. The goal of this sensitivity study is to determine the ranges of comparison model particle mixtures and total optical depths that give acceptable matches to the 13 climatologically representative atmospheric air mass types listed in Table 2.

3.1. Testing Agreement Between "Measurements" and Comparison Models

Over ocean the MISR retrieval makes use of up to 18 measurements: nine angles at each of the two longest MISR wavelengths (bands 3 and 4, centered at 672 and 867 nm, respectively), where the water surface is darkest. We define four test variables to decide whether a comparison model is consistent with the measurements. Each is based on the χ^2 statistical formalism [e.g., *Bevington and Robinson*, 1992].

One test variable weights the contributions from each observed reflectance according to the slant path through the atmosphere of the observation

$$\chi^2_{\text{abs}} = \frac{1}{N \langle w_k \rangle} \sum_{l=3}^{4} \sum_{k=1}^{9} \frac{w_k [\rho_{\text{meas}}(l, k) - \rho_{\text{comp}}(l, k)]^2}{\sigma^2_{\text{abs}}(l, k; \rho_{\text{meas}})}, \quad (2)$$

where ρ_{meas} is the simulated "measurement" of atmospheric equivalent reflectance, and ρ_{comp} is the simulated equivalent reflectance for the comparison model. (We define equivalent reflectance as the radiance multiplied by π and divided by the exoatmospheric solar irradiance at normal incidence.) Values l and k are the indices for wavelength band and camera, N is the number of measurements included in the calculation, w_k are weights, chosen to be the inverse of the cosine of the viewing angle appropriate to each camera k (i.e., the weights are proportional to the air mass through which the camera views), $\langle w_k \rangle$ is the average of weights for all the measurements included in the summation; $\sigma_{\text{abs}}(l, k; \rho_{\text{meas}})$ is the absolute calibration uncertainty in the equivalent reflectance for MISR band l and camera k. The nominal value of σ_{abs} for MISR falls between 0.03 for a target with equivalent reflectance of 100% and 0.06 for an equivalent reflectance of 5%, in all channels [*Diner et al.*, 1998a]. For the simulations we model σ_{abs} as varying linearly with equivalent reflectance over this range.

The χ^2_{abs} alone reduces 18 measurements to a single statistic; χ^2_{abs} emphasizes the absolute reflectance, which depends heavily on aerosol optical depth for bright aerosols over a dark surface. However, there is more information in the measure-

ments that we can use to improve the retrieval discrimination ability.

A second χ^2 test variable emphasizes the geometric properties of the scattering, which depend heavily on particle size and shape. For the χ^2_{geom} test variable, each spectral measurement is divided by the corresponding spectral measurement in the nadir camera:

$$\chi^2_{geom} = \frac{1}{N\langle w_k \rangle}$$

$$\cdot \sum_{l=3}^{4} \sum_{\substack{k=1 \\ k \neq nadir}}^{9} \frac{w_k \left[\frac{\rho_{meas}(l, k)}{\rho_{meas}(l, nadir)} - \frac{\rho_{comp}(l, k)}{\rho_{comp}(l, nadir)} \right]^2}{\sigma^2_{geom}(l, k; \rho_{meas})}. \quad (3a)$$

Here σ^2_{geom} (a dimensionless quantity) is the uncertainty in the camera-to-camera equivalent reflectance ratio, derived from the expansion of errors for a ratio of measurements ($\sigma^2(f(x, y)) = (\partial f/\partial x)^2 \sigma^2_x + (\partial f/\partial y)^2 \sigma^2_y$ [e.g., *Bevington and Robinson*, 1992]):

$$\sigma^2_{geom.cal}(l, k; \rho_{meas}) = \frac{\sigma^2_{cam}(l, k; \rho_{meas})}{\rho^2_{meas}(l, nadir)}$$

$$+ \frac{\sigma^2_{cam}(l, nadir; \rho_{meas})\rho^2_{meas}(l, k)}{\rho^4_{meas}(l, nadir)}, \quad (3b)$$

$\sigma_{cam}(l, k; \rho_{meas})$ is the contribution of (band l, camera k) to the camera-to-camera relative calibration reflectance uncertainty; σ_{cam} is nominally one-third the corresponding value of σ_{abs} for the MISR instrument [*Diner et al.*, 1998a]. Note that σ_{cam} includes the effects of systematic calibration errors for ratios of equivalent reflectance between cameras, as well as random error due to instrument noise, though the latter has been neglected in these simulations, based on the high signal-to-noise ratio demonstrated during MISR camera testing [*Bruegge et al.*, 1998].

Similarly, we define a spectral χ^2 as

$$\chi^2_{spec} = \frac{1}{N\langle w_k \rangle} \sum_{k=1}^{9} \frac{w_k \left[\frac{\rho_{meas}(band4, k)}{\rho_{meas}(band3, k)} - \frac{\rho_{comp}(band4, k)}{\rho_{comp}(band3, k)} \right]^2}{\sigma^2_{spec}(l, k; \rho_{meas})},$$

$$(4a)$$

with

$$\sigma^2_{spec}(l, k; \rho_{meas}) = \frac{\sigma^2_{band}(l, k; \rho_{meas})}{\rho^2_{meas}(band3, k)}$$

$$+ \frac{\sigma^2_{band}(band3, k; \rho_{meas})\rho^2_{meas}(l, k)}{\rho^4_{meas}(band3, k)}, \quad (4b)$$

$\sigma_{band}(l, k; \rho_{meas})$ is the contribution of (band l, camera k) to the band-to-band relative calibration reflectance uncertainty; σ_{band} is nominally one-third the corresponding value of σ_{abs} for the MISR instrument.

We include a maximum deviation test variable that is the single largest term contributing to χ^2_{abs} (see equation (2)):

$$\chi^2_{max\_dev} = \text{Max}_{l,k} \frac{[\rho_{meas}(l, k) - \rho_{comp}(l, k)]^2}{\sigma^2_{abs}(l, k; \rho_{meas})}. \quad (5)$$

All the other test variables are averages of up to 18 measurements. $\chi^2_{max\ dev}$ makes the greatest use of any band-specific or scattering-angle-specific phenomenon, such as a rainbow or a spectral absorption feature, in discriminating between the measurements and the comparison models.

3.2. Evaluating the χ^2 Test Variables

We defined four dependent variables to be used in comparing measurements with models (χ^2_{abs}, χ^2_{geom}, χ^2_{spec}, and $\chi^2_{max\ dev}$). Since each χ^2 variable is normalized to the number of channels used, they are "reduced" χ^2 quantities, and a value less than or about unity implies that the comparison model is indistinguishable from the measurements. Values larger than about 1 imply that the comparison model is not likely to be consistent with the observations. In more detail, $\chi^2 < 1$ means that the average difference between the measured and the comparison quantities is less than the associated measurement error. If the quantity in the numerator of a reduced χ^2 variable definition with 17 degrees of freedom is sampled from a population of random variables, an upper bound of 1 corresponds formally to an average confidence of about 50% that we are not rejecting a comparison model when in fact it should be accepted; for an upper bound of 2, the confidence increases to almost 99% [*Bevington and Robinson*, 1992]. This is not strictly true for the "χ^2" variables defined here. They are actually the averages of correlated measurements from multiple bands and cameras, though each term contributing to these variables may itself be distributed as χ^2. So a given upper bound is likely to be a less stringent constraint than the formalism implies.

To illustrate the values of the test variables, we developed a color bar with three segments: a logarithmic segment for values between 10^{-5} and 1 depicted in shades of blue, a logarithmic segment for values between 5 and 10^4 depicted in shades of red, and a linear segment shown in light green, yellow, and orange shades for the intermediate values [*Kahn et al.*, 1998]. Thus red shades in the figures indicate situations where the model is clearly distinguishable from the measurement, whereas blue shades indicate that the model is indistinguishable from the measurement. Black is reserved for exact agreement between model and measurement, which can occur in this study because we are working with simulated observations. Note that the color table has been designed so that if the figures are photocopied in black and white, first-order information about the ability to distinguish among models is preserved.

4. Sensitivity to Natural Aerosol Mixes

We are now ready to assess the MISR retrieval of climatologically probable aerosol mixtures over dark water. Table 2 defines the extensive comparison space of five mixing groups which covers every proportion of four-component mixtures for the climatologically probable combinations of six component particles. The sensitivity study is accomplished by identifying the ranges of mixtures within the comparison space which give satisfactory matches to each of the 13 representative air mass types identified in section 2.1 and also given in Table 2. A narrow range indicates that MISR retrievals should be good at identifying that air mass type. We look first at simulations for air masses having moderate aerosol optical depth. We next examine how sensitivity is affected by low optical depth. Once the general patterns for all 13 air mass types have been characterized and explained in terms of the physical properties of the component particles, we briefly discuss the effects of thin cirrus and of the geographic latitude of observation upon the results.

4.1. MISR Sensitivity to 13 Representative Air Mass Types, Based on Five Climatologically Probable Mixing Groups

We begin this section by taking a close look at several specific cases and then examine summaries of the entire comparison space. Plate 4 shows the results of tests between simulated MISR measurements for an atmosphere with aerosol air mass type 2a (Table 2) and the 1771 comparison model mixtures that comprise mixing group 2 (dusty maritime + coarse dust). The optical depth in MISR band 2 is set to 0.5 for both the atmosphere and the comparison models in this first example, and typical MISR midlatitude geometry has been adopted; we subsequently vary the aerosol optical depth systematically over the entire range from 0.0 to 1.0. The comparison model cases are arranged in a tetrahedron, and Plate 4 shows slices through this tetrahedron covering the interesting part of the space. Each pixel is divided into five fields. The upper left subpixel is colored with the result of the χ^2_{abs} test, the upper right has the result of the χ^2_{geom} test, the lower left shows the $\chi^2_{max\_dev}$ test, and the lower right contains the χ^2_{spec} test, each using the color bar described in section 3.2. The background is colored with the result of the most constraining of these four tests (the one with the highest value), since, if any one of the tests indicates that the comparison model does not match the observation, the comparison model must be rejected. We call this value χ^2_{max}.

Only four planes in Plate 4 have pixels with $\chi^2_{max} < 1$. So if we use this as the criterion for accepting a comparison model, the fraction of the total optical depth contributed by coarse mode dust is constrained to fall between 5% and 20%, since no models having coarse mode dust fraction outside this range match the observations. Similarly, the sulfate particle mixing ratio is confined to the range 50–55%, accumulation mode dust must fall between 5 and 35%, and sea salt is constrained between 5 and 25%. Plate 4 also indicates the correlations among acceptable fractions for each component. The actual composition for air mass type 2a is 10% coarse mode dust, 52% sulfate, 21% accumulation mode dust, and 17% sea salt. In this case, the MISR retrieval constrains all the component particle types in the mixture to within 15% of their true optical depth mixing ratios, and the best constraint is better than 5%.

Plates 5a–5d show sections through the tetrahedral comparison space for mixing group 4 (carbonaceous + dusty continental), for an atmosphere with an aerosol composition given by air mass type 4a (Table 2). Four planes with constant coarse mode dust mixing ratio, ranging from 0 to 15%, are presented. In this case, the $\chi^2_{max} < 1$ criterion yields solutions only for coarse mode dust between 0 and 10% mixing ratio, based on MISR band 2 optical depth contribution, and for accumulation mode dust between 20 and 25%. The sulfate and carbonaceous particles form a mixing line; models having as much as 70% sulfate (and 0% carbonaceous particles) or as little as 40% sulfate (and 40% carbonaceous particles) meet the acceptance criterion. For these mixtures of particles over a dark water surface, a simulated MISR retrieval using the red and near-infrared bands and all nine angles cannot distinguish sulfates, which are "medium, spherical, nonabsorbing" particles, from carbonaceous, which are "medium, spherical, absorbing" particles (Table 3). However, the sum of the fractional contributions to optical depth of sulfate and carbonaceous particles is always around 75%. This is close to the true value, the sum of 61% sulfate and 13% carbonaceous particle-mixing ratios.

A similar result appears in Plates 5e–5h, which examines the sensitivity of MISR to an atmosphere having aerosol compo-

sition given by air mass type 4c, in the tetrahedral comparison space for mixing group 4. Air mass type 4c contains only 22% sulfate and 11% carbonaceous particle optical depth contributions, along with 51% accumulation mode dust and 16% coarse mode dust. Using the $\chi^2_{max} < 1$ criterion, acceptable matches are found for coarse mode dust between 10 and 20%, and accumulation mode dust from 45 to 55%, reflecting the larger dust contribution for air mass type 4c than for type 4a. Again, sensitivities are around ±10% in optical depth mixing ratio, surrounding the expected value, except for sulfate and carbonaceous aerosols, which form a mixing line.

Figure 2 gives a more extensive though less detailed picture of MISR sensitivity to all 13 representative air mass types, as compared with every combination on 5% tetrahedral grids for all five mixing groups. There are 13 columns of whisker plots, one for each representative air mass type in Table 2. The first five rows are comparisons of the air mass types with each of the five mixing groups. The horizontal axis for each whisker plot allows six positions, one for each component particle in this study. The vertical axis shows the range from 0 to 1, of the component's fractional contribution to the total optical depth. There are no more than four whiskers in each plot, corresponding to the components of the relevant mixing group. Each whisker indicates the largest and smallest fractional contribution to the total optical depth of that component, for any comparison model in the mixing group that meets the criterion $\chi^2_{max} < 1$. Longer whiskers indicate that acceptable comparison models span a wider range of optical depth mixing ratios. Note that correlations among component particles, such as the relationship between sulfate and carbonaceous particles illustrated in Plate 5, are not shown in Figure 2. However, an "x" on each whisker indicates the component's optical depth mixing ratio for the comparison model in the relevant mixing group having the lowest value of χ^2_{max}. The last row of plots shows with a "plus" the actual fractions of component particles contributing to the air mass type for each column.

For Figure 2 the total atmospheric column optical depth, and that of all comparison models, is set to 0.5, and typical MISR midlatitude geometry is used. Scanning down the columns, there are no matches at all for any of the seven "maritime" air masses in the "continental" mixing groups (groups 4 and 5). This illustrates how distinctive sea-salt particles (large, spherical, Table 3) appear to MISR when the background is dark water. Similarly, there is only one match for any "continental" air mass in the three "maritime" mixing groups. This match is for air mass 4b in mixing group 1. The acceptable comparison model has 40% accumulation mode dust, which is similar to the air mass value, and a combination of sulfate and carbonaceous particles that apparently accounts for the medium, spherical particles in the air mass; and the chosen model contains none of the distinctive sea salt available in the mixing group but absent from the air mass. The χ^2_{max} for this model is 0.958.

Further examination of Figure 2 reveals that sensitivities to all components are within 10–20% or better of the expected values, except for the redundancy between sulfates and carbonaceous particles. Discrimination between spherical and nonspherical particles is so strong that there are no matches for air masses 2a and 2b, which contain accumulation and coarse mode dust, in mixing group 3, which lacks both of these particle types. Continental air mass types produce very similar ranges of sulfates, accumulation mode dust, and carbonaceous particles in both continental mixing groups. However, the re-
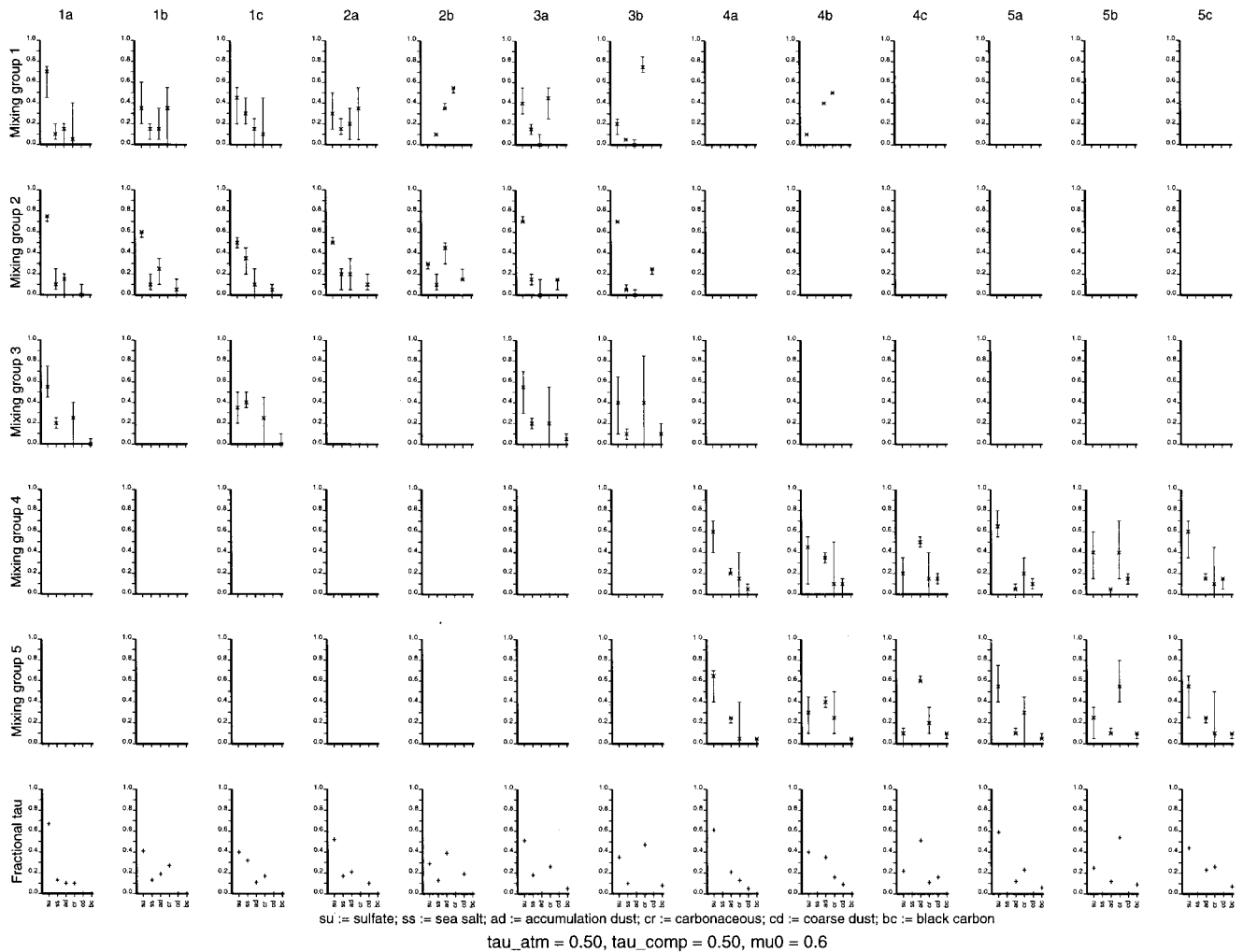
Figure 2. Whisker plot matrix shows MISR sensitivity to all 13 representative air mass types, as compared with every combination on 5% tetrahedral grids for all five mixing groups. Each column contains plots for one air mass type in Table 2. The first five rows are for each of the mixing groups in Table 2. The horizontal axis for each whisker plot allows six positions, one for each component particle in this study (Tables 1 and 3). The vertical axis in each plot indicates the fraction of column optical depth in MISR band 2 contributed by a component. Each plot summarizes the comparisons between an atmosphere with the aerosol mixture defined by one air mass type and all 1771 comparison models in one mixing group. Whiskers are drawn spanning the upper and lower limits of fractional contribution of each component in the mixing group, for any model that meets the criterion $\chi^2_{max} < 1$. Component particle mixing ratios for the comparison model yielding the smallest value of χ^2_{max} are marked by "x" on each whisker. Row 6 plots indicate with "+" the fractions of components in the air mass types. For this plot matrix the total column optical depth in MISR band 2 is set to 0.5 for all atmospheres and comparison models, and cosine of the solar zenith angle is set to 0.6, a typical MISR midlatitude situation. See text for further details.

trievals find acceptable matches with either black carbon (small, absorbing) or coarse mode dust (large, nonspherical, absorbing), when tested against atmospheres containing aerosols from the continental air masses in our climatology. These air masses contain 20% or less of black carbon or coarse mode dust components, the apparent limit on MISR sensitivity to particle properties in climatologically probable mixtures, for the dark water, two-spectral-band retrievals simulated here.

4.2. Sensitivity to Optical Depth and to Air Mass Type at Low Optical Depth

We varied the optical depths of the atmospheres and comparison models independently and assessed the retrieval re-

sults. From the generic sensitivity study [*Kahn et al.*, 1998] we know that sensitivity decreases with decreasing atmospheric total column optical depth. Following the results of that paper, we anticipate that regardless of composition, comparison models differing in total column optical depth by 20% or more should not match the atmosphere. There is a difference, however, between the generic and the climatological retrievals. The generic retrieval involves only one set of effective, column-weighted particle phase functions and indices of refraction for each atmosphere and each comparison model. The climatological retrieval is free to mix properties of up to four component particles, and occasionally, the individual particle phase functions combine to produce spurious matches with larger optical
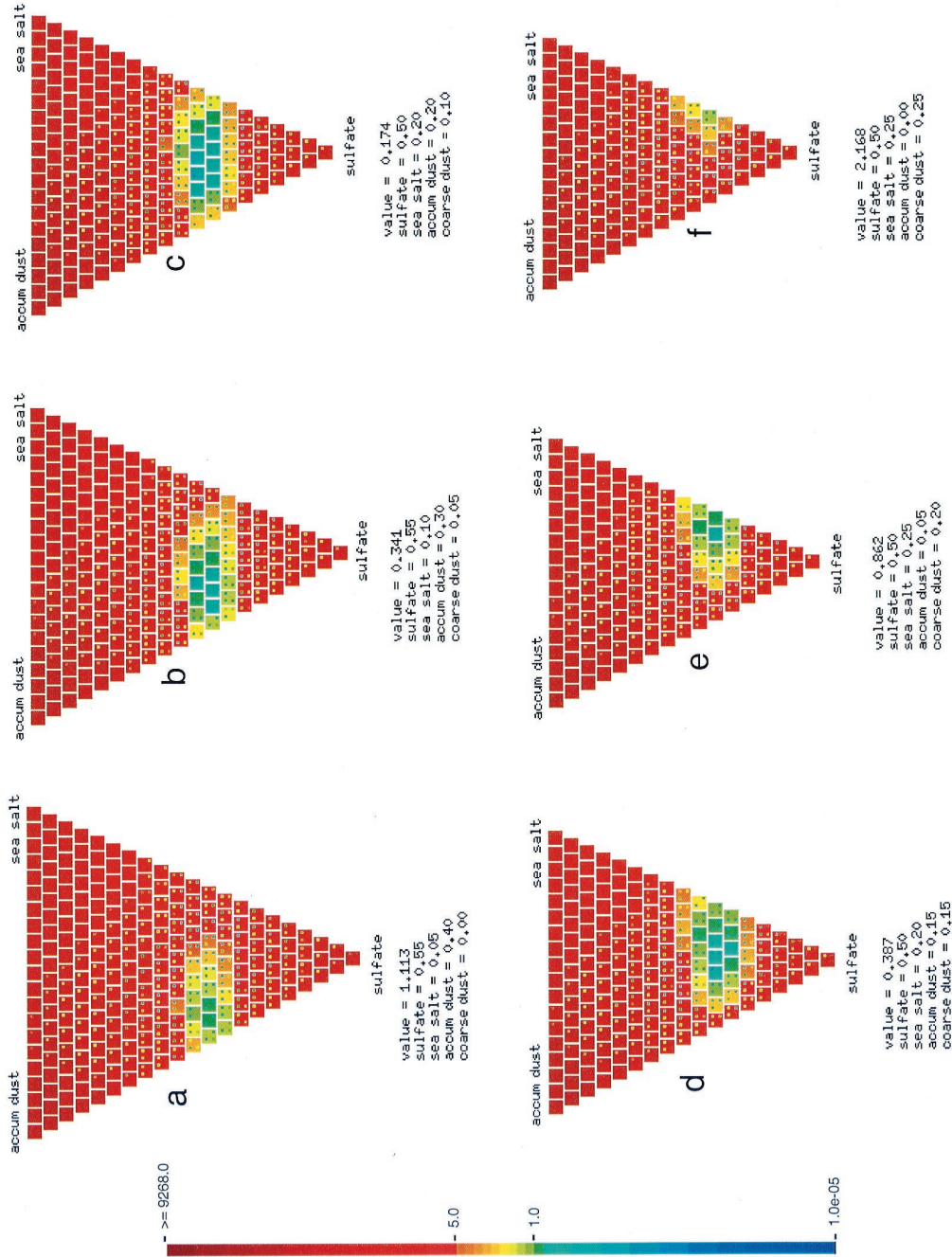
Plate 4. Example of sections through a tetrahedral comparison matrix. Air mass type 2a (Table 2) defines the aerosol composition of the atmosphere, and the comparison models are all 1771 combinations of sulfate, sea salt, accumulation mode dust, and coarse mode dust, in 5% increments, which define mixing group 2. In this figure, the optical depth in MISR band 2 is set to 0.5 for both the atmosphere and the comparison models, and typical MISR midlatitude geometry is adopted. Shown here are six planes with constant coarse mode dust fraction, corresponding coarse mode dust of (a) 0%, (b) 5%, (c) 10%, (d) 15%, (e) 20%, and (f) 25%. Each pixel is divided into five fields; the four subpixels are colored to indicate the results of four chi-square tests comparing the atmosphere and one comparison model. The background is colored with the result of the largest (most sensitive) of the four tests. A blue pixel indicates that within instrument uncertainty, the associated comparison model must be accepted. Below each section are listed the maximum test value (χ^2_{max}), and the corresponding fraction of each component, for the comparison model having the smallest χ^2_{max}, suggesting that this model matches the atmosphere most closely. See text for further details.
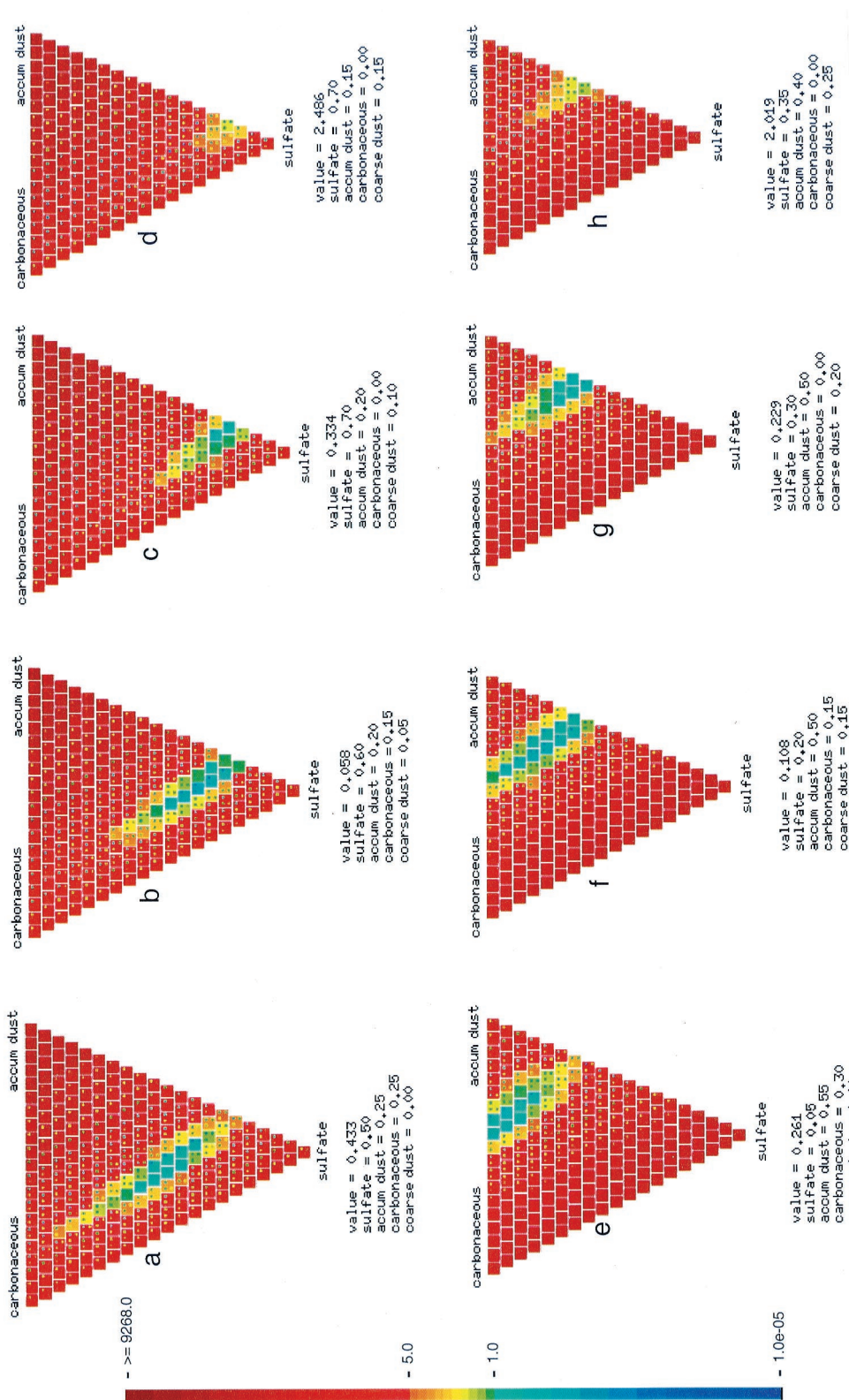
Plate 5. (a–d) Same as Plate 4 but for an atmosphere with aerosol composition given by air mass type 4a (Table 2) and comparison models defined by mixing group 4 (carbonaceous + dusty continental, Table 2). Shown here are four planes having constant coarse mode dust fraction, corresponding to (a) 0%, (b) 5%, (c) 10%, and (d) 15%. (e–h) Same as Plates 5a–5d but with the atmosphere defined by air mass type 4c. The four planes shown are sections with constant coarse mode dust fraction, corresponding to (e) 10%, (f) 15%, (g) 20%, and (h) 25%. Air mass type 4c contains 39% less sulfate, 30% more accumulation mode dust, and 11% more coarse mode dust than air mass type 4a.

depth differences. Fortunately, these tend to be isolated solutions, whereas there is usually a range of acceptable models surrounding the values for a correct solution, as shown in Figure 2. We further discuss spurious solutions below.

When the 13 atmospheres have optical depth 0.5, there are no matches for comparison models having optical depths less than 0.4, for any mixing group. Nor are there any matches for comparison models with optical depths greater than 0.6, except for several isolated cases. The exceptions involve black carbon, which is in the comparison models but not in the atmospheres for these cases, and accumulation mode dust, which is in the atmospheres but not the comparison models. Increased black carbon fraction substitutes for accumulation mode dust and keeps the absolute reflectance low, while small adjustments in sea salt, sulfate, and carbonaceous fractions complete the matches.

The phase function plots for individual particle types in Figure 1 provide some insight into these spurious cases. The black carbon phase function is relatively flat over the range of scattering angles viewed by the forward cameras (about 60° to 100°) and aft cameras (about 150° to 160°). Since the phase function for accumulation mode dust, which is present in the atmospheres but absent from the comparison models, is also fairly flat over these angles, matches are possible.

Multiple scattering accounts for between 50 and 70% of the signal in all these cases, so there are limits as to how far it is useful to carry interpretations based on reasoning from single scattering. We conclude that we can account qualitatively for the trends in the spurious matches. If this were a retrieval involving real data, such a match would be suspect because (1) only a few isolated cases give matches for each comparison model optical depth, rather than 5% to 20% ranges of fractional amounts, as occur for true solutions, and (2) the mixing ratio of black carbon, 20% or more, falls significantly outside the climatologically probable range.

The situation is far simpler for atmospheres having total column optical depth 0.5 and comparison models having lower optical depths. There is no particle in the climatology with a relatively flat scattering phase function that can increase reflectances, as black carbon lowers them when the comparison model optical depth is higher. For comparison models having optical depth below 0.4, there are no matches at all.

When the total atmospheric column aerosol optical depth falls to between 0.1 and 0.2 in MISR band 2, information about particle properties decreases, the number of matches grows, and some of the substitutions occur more readily than at higher optical depth. For example, with atmospheric and comparison model optical depths at 0.2, solutions are found in mixing group 2 (which is maritime) for all six continental air mass types, though the amount of sea salt in the solutions is usually either 0 or 5%. In other cases, combinations of accumulation mode dust and carbonaceous particles in a comparison model can account for the contributions of coarse mode dust in the atmosphere at these low overall optical depths.

However, even at low optical depths the ability to discriminate large, spherical particles (sea salt), nonspherical particles (accumulation and coarse mode dust), and small, dark particles (black carbon) is preserved, to within 20% of the component's true contribution to the total optical depth. In addition, sensitivity to optical depth itself remains high. For an atmosphere having 0.2 total column optical depth, there are no matches at all when the comparison model optical depths are 0.15 or lower, or when they are higher than 0.35. As with the more optically thick atmospheres, spurious matches can occur when comparisons are made with models having higher optical depth and containing black carbon (mixing groups 3 and 5). Once again, in all these cases, black carbon accounts for a climatologically high fraction of the total optical depth. Such cases would be suspect in an actual retrieval.

4.3. Sensitivity Issues Related to Thin Cirrus and to Geographic Latitude

The MISR data processing algorithms use several cloud-detection approaches to eliminate observations containing clouds [e.g., *Diner et al.*, 1998a; *Gao and Kaufman*, 1995]. Although we expect these masks to be effective over a wide range of natural conditions, they are unlikely to be reliable when the cirrus normal optical depth is less than a few tenths at midvisible wavelengths.

Thin cirrus is fundamentally different from the component particles considered in previous sections. There are common mechanisms that form optically thin hazes of cirrus ice crystals at most latitudes. Climatological constraints on the spatial and temporal distribution of thin cirrus are so loose that by including it, we create an additional dimension in the sensitivity study.

We performed a preliminary study of four-component mixtures that include thin cirrus, assuming cirrus microphysical properties from the fractal model of *Mishchenko et al.* [1996], listed in Table 3 and shown in Figure 1. A new set of mixing groups was created, containing both cirrus and sulfate components, along with sea salt for maritime groups, accumulation mode dust for the continental groups, and one of the remaining entries in Table 1 as the fourth component. New air mass types were defined, based loosely on the patterns in Table 2, but containing 10, 20, and 50% cirrus contributions to the total column aerosol optical depth.

The study involved three additional sets of tests: atmospheres containing cirrus versus comparison models without cirrus, atmospheres without cirrus against comparison models containing cirrus, and atmospheres containing cirrus against comparison models containing cirrus. Most of the behavior follows patterns described in sections 4.1 and 4.2.

In nearly all cases the retrieval can distinguish thin cirrus from other component particles if the total column aerosol optical depth is greater than about 0.2 and the cirrus contribution is more than about 20%. The ability of MISR to identify aerosol air mass types is significantly reduced when cirrus is present, but the sensitivity to total aerosol optical depth is not diminished. A more extensive study of thin cirrus sensitivity, one that incorporates several cirrus particle models as well as comparisons with MISR observations, will be the subject of a future paper.

Since the range of scattering angles observed by MISR varies with latitude, we also expanded the sensitivity study to include high- and low-latitude cases. At high latitudes the range of scattering angles sampled by MISR increases, extending from about 40° to 160°. The patterns are very similar to those at midlatitudes; the lengths of whiskers are shorter in some cases but not significantly so relative to the ranges of uncertainty. At low latitudes, scattering angle coverage is limited to between about 105° and 165°. Whisker lengths are longer in some cases, and a few more coincidental matches occur, but the conclusions of this and previous sections remain intact.

5. Discussion and Conclusions

In earlier theoretical work we performed generic retrieval simulations for a MISR-like instrument. Such retrievals make a minimum of assumptions about the particles present and seek column-averaged, cross-section-weighted mean aerosol properties. The results provide insight into the information content of the observations. We found that for natural ranges of particle properties, under good observing conditions, the MISR retrieval can make about a dozen distinctions based on particle size (small, medium, large), shape (spherical and randomly oriented nonspherical), and composition (absorbing and nonabsorbing), along with estimates of aerosol column optical depth.

A limitation of the generic retrieval approach is that cross-section-weighted mean aerosol properties are difficult to compare with in situ and field measurements, and with the results of any physically based aerosol transport model, since these describe the behavior of mixtures of component particles. The current paper explores climatological retrievals for simulated MISR data. Such retrievals constrain the proportions of individual components in climatologically probable mixtures. We conclude that multiangle, multispectral imaging contains enough information about particle properties to warrant adopting this retrieval approach as well.

Since the value of a climatological retrieval depends on the quality of an assumed climatology, we base our assumptions on results from some of the best available global, monthly aerosol transport models. Our analysis shows that the entire global, monthly data set, aggregated from transport models for the six most common component particles, can be represented by a climatology containing only five mixing groups, each composed of all possible proportions of four externally mixed components. The mixing groups define the climatological retrieval comparison space. We also find that within each mixing group, the climatologically probable mixtures cluster into only two or three representative air mass types, having specific proportions of the four components in that group. For the sensitivity study, these representative air mass types characterize the sample atmospheres that are tested against the comparison space. The mixing group and representative air mass type results are summarized in Table 2 and Plate 1.

To complete the climatology, we must assume microphysical properties for each component aerosol (Table 3). The values used here were obtained from standard sources and reflect the characteristic differences among component particles. However, detailed microphysical properties of component particles vary with source region and air mass meteorological history. When performing retrievals with MISR data, we anticipate using additional constraints from in situ and field measurements whenever possible to reduce the uncertainties.

On the basis of midlatitude simulations, for the assumed climatology, good viewing conditions, and moderate aerosol optical depth (nominally 0.5 at 0.56 μm wavelength), MISR can retrieve sea salt (large, spherical particles) and accumulation mode dust (medium, nonspherical particles) to within 20% of the true mixing ratio or better. This is sufficient to distinguish maritime from continental aerosol air masses. MISR retrievals over dark water, using nine angles and the red and near-IR channels, are not good at distinguishing sulfates (medium, spherical, nonabsorbing) from carbonaceous particles (medium, spherical, absorbing); however, the sum is retrieved to within 20% of the true mixing ratio or better.

Coarse mode dust and black carbon particles contribute less than 20% to the total column aerosol optical depth everywhere in the climatology. Though models having the correct composition usually yield the lowest χ^2_{max}, comparison models with adjusted amounts of other components can usually be found to meet the acceptance criterion for atmospheres containing the less abundant particles.

In spite of the added flexibility offered by the climatological retrieval in allowing mixtures of components having different single-scattering phase functions, constraints on total aerosol optical depth are nearly as tight as those for the generic retrieval. With an atmospheric aerosol optical depth of 0.5 no comparison models having optical depth less than 0.4 or greater than 0.75 match any of the atmospheres. The matching comparison models having optical depths greater than 0.60 all contain large fractions of black carbon, and most are isolated solutions that arise from fortuitous combinations of particle-scattering phase functions. In actual retrievals, such cases would be suspect, because (1) retrieved component mixing ratios for true solutions are not isolated; they typically span a range of 5–20%, and (2) mixtures containing 20% or more black carbon are climatologically improbable.

When the total atmospheric aerosol column optical depth is reduced to 0.2, the constraints are looser than for the 0.5 cases, and some substitutions of component particles occur more readily. However, the ability to distinguish large, spherical particles (sea salt), nonspherical particles (accumulation and coarse mode dust), and small, dark particles (black carbon) is preserved, at least to within 20% or better of the expected values; and even with reduced sensitivity to particle microphysical properties, the total aerosol optical depth is constrained to 0.05 or better, if one rejects cases having implausibly large fractions of black carbon or coarse mode dust.

We can relate the climatological retrieval approach developed here to other satellite aerosol retrievals. The MISR climatological retrieval looks at five mixing groups, each composed of four component particles in all possible combinations. Each mixing group can be represented by a tetrahedron, as described in sections 2.1 and 4.1.

The AVHRR phases 1 and 2 aerosol retrieval algorithms [*Stowe et al.*, 1997] can be viewed as climatological retrievals that interpret one-channel measurements using one vertex of one tetrahedron as the comparison space. For the phase 2 algorithm, a medium spherical (sulfate-like) particle type is assumed, having a lognormal size distribution with characteristic radius 0.1 μm, width 2.03, and index of refraction $1.4 - 0.0i$. For interpreting single-channel observations the aerosol climatology developed for the MISR analysis seems to support this choice; sulfates are the only particles common to all air mass types, and they frequently account for a substantial fraction of the column aerosol optical depth, particularly over ocean.

Many two-channel AVHRR algorithms are cast as generic rather than climatological retrievals [e.g., *Durkee et al.*, 1991; *Stowe et al.*, 1997; *Mishchenko et al.*, 1999]. These produce aerosol column optical depth, and a constraint on column mean, cross-section-weighted particle size from a continuum of possible values, for assumed particle size distribution function, particle shape, and indices of refraction; but here the line between generic and climatological retrievals blurs. Having assumed size distribution function, shape, and indices of refraction, the ratio of two-component particles can be uniquely calculated from a retrieved size constraint such as a value of

the Angstrom coefficient. Attempts are made in these studies to interpret the size constraints resulting from the retrievals in terms of climatologically probable components.

A retrieval developed for AVHRR [*Higurashi and Nakajima*, 1998], and also applied to the OCTS instrument [*Nakajima and Higurashi*, 1998; *Nakajima et al.*, 1999], takes a climatological approach, solving explicitly for the ratio of small to large particle components along with aerosol column optical depth. This retrieval assumes two lognormal distributions of spherical particles having characteristic radii 0.17 and 3.44 μm, and for the OCTS case, widths 1.3 and 2.75, respectively. The index of refraction is set to $1.5 - 0.005i$ for all particles. This approach amounts to using the edge of one tetrahedron as the comparison space. The components chosen are a medium spherical particle (corresponding to the carbonaceous or sulfate components in the MISR climatology) and a large spherical particle (similar to the MISR sea salt, though larger). The results of the present study seem to fit well with this selection. Of the six components in the MISR retrieval, sulfate and carbonaceous particles are difficult for satellite remote sensing instruments to distinguish over dark water. Spherical and nonspherical particles are difficult to distinguish for instruments lacking multiangle capability, and sensitivity to small, dark particles (black carbon) over dark water is not so high as for other components. This collapses the MISR six-component comparison space down to one large spherical and one medium spherical component.

The standard dark water aerosol retrieval for the multispectral, nadir-looking Moderate-Resolution Imaging Spectroradiometer (MODIS) instrument, flying on the Terra platform along with MISR, is a hybrid of generic and climatological approaches [*Tanre et al.*, 1997]. The algorithm solves for aerosol column optical depth and the ratio of contributions from pairs of lognormally distributed components, one medium spherical, the other, large spherical. However, in addition, the retrieval selects a best fit medium spherical component from among five options having incrementally different radii, widths, and indices of refraction. Similarly, the large spherical component is selected from among six options.

From an aerosol climatology perspective, one qualitatively new contribution of MISR is an ability to distinguish spherical from nonspherical particles. We are driven to create a comparison space of five four-component mixing groups so we can explicitly include climatologically important coarse dust and black carbon components, to which MISR has some sensitivity, but which are rarely among the two or three most abundant particles in natural air masses. By reporting the range of acceptable solutions over an extensive, climatologically based comparison space, the MISR climatological retrieval distinguishes among aerosol air mass types with passive remote sensing observations.

In this series of MISR aerosol retrieval papers, we have sorted through an enormous amount of simulated data. We have identified patterns in the MISR sensitivity to atmospheric aerosols using both a column-average-particle "generic" approach and a retrieval strategy for aerosol mixtures which relies on a climatology of component particles having assumed microphysical properties. The retrievals were performed using the MISR red and near-infrared channels, at all nine look angles, over dark water. Enhancements to these retrieval strategies are possible, such as including data from the MISR blue or green channels, if issues of ocean surface reflectance at these wavelengths and increased sensitivity to the vertical dis-

tribution of aerosols can be addressed. We may find ways to improve aerosol retrieval sensitivity by incorporating data from other instruments, such as longer wavelength channels from MODIS.

However, it is time to look at real data. With instrument observations, uncertainties introduced by specific attributes of the environment will need to be considered: the vertical distribution of aerosols, the surface bidirectional reflectance function, the actual physical properties of the aerosols and any cirrus ice crystals present, and variability of surface and aerosol properties within the scene. Where possible, we will rely on in situ and field measurements to help constrain the solution space. Analysis of observations from AirMISR, the aircraft version of our multiangle instrument [*Diner et al.*, 1998b], is the subject of continuing work [*Kahn et al.*, 2000]; and we are just beginning to look at data from MISR itself.

References

Abdou, W. A., J. V. Martonchik, R. Kahn, R. West, and D. Diner, A modified linear-mixing method for calculating atmospheric path radiances of aerosol mixtures, *J. Geophys. Res.*, *102*, 16,883–16,888, 1997.

Andreae, M. O., Climatic effects of changing atmospheric aerosol levels, in *World Survey of Climatology*, vol. 16, *Future Climates of the World*, A. Henderson-Sellers (Ed.), pp. 341–392, Elsevier Sci., New York, 1995.

Bevington, P. R., and D. K. Robinson, *Data Reduction and Error Analysis for the Physical Sciences*, 2nd ed., 328 pp., McGraw-Hill, New York, 1992.

Bruegge, C. J., V. G. Duval, N. L. Chrien, R. P. Korechoff, B. J. Gaitley, and E. B. Hochberg, MISR prelaunch instrument calibration and characterization results, *IEEE Trans. Geosci. Remote Sens.*, *36*, 1186–1198, 1998.

Charlson, R. J., S. Schwartz, J. Hales, R. Cess, J. Coakley Jr., J. Hansen, and D. Hofmann, Climate forcing by anthropogenic aerosols, *Science*, *255*, 423–430, 1992.

Chin, M., D. J. Jacob, G. M. Gardner, P. A. Spiro, M. Foreman-Fowler, and D. L. Savoie, A global three-dimensional model of tropospheric sulfate, *J. Geophys. Res.*, *101*, 18,669–18,690, 1996.

Cusack, S., A. Slingo, J. M. Edwards, and M. Wild, The radiative impact of a simple aerosol climatology on the Hadley Centre atmospheric GCM, *Q. J. R. Meteorol. Soc.*, *124*, 2517–2526, 1998.

d'Almeida, G. A., P. Koepke, and E. P. Shettle, *Atmospheric Aerosols: Global Climatology and Radiative Characteristics*, A. Deepak, Hampton, Va., 1991.

Deschamps, P. Y., F. M. Breon, M. Leroy, A. Podaire, A. Brichaud, J. C. Buriez, and G. Seze, The POLDER mission: Instrument characteristics and scientific objectives, *IEEE Trans. Geosci. Remote Sens.*, *32*, 598–615, 1994.

Diner, D. J., et al., Multiangle Imaging SpectroRadiometer (MISR) description and experiment overview, *IEEE Trans. Geosci. Remote Sens.*, *36*, 1072–1087, 1998a.

Diner, D. J., et al., The Airborne Multi-angle Imaging SpectroRadiometer (AirMISR): Instrument description and first results, *IEEE Transact. Geosci. Remote Sens.*, *36*, 1339–1349, 1998b.

Durkee, P. A., F. Pfeil, E. Frost, and R. Shema, Global analysis of aerosol particle characteristics, *Atmos. Environ., Ser. A*, *25*, 2457–2471, 1991.

Gao, B.-C., and Y. J. Kaufman, Selection of the 1.375-μm MODIS channel for remote sensing of cirrus clouds and stratospheric aerosols from space, *J. Atmos. Sci.*, 52, 4231–4237, 1995.

Grant, I. P., and G. E. Hunt, Solution of radiative transfer problems using invariant S_n method, *Mon. Not. R. Astron. Soc.*, 141, 27–41, 1968.

Hanel, G., The properties of atmospheric aerosol particles as functions of relative humidity at thermodynamic equilibrium with the surrounding moist air, *Adv. Geophys.*, 19, 73–188, 1976.

Hansen, J. E., and L. D. Travis, Light scattering in planetary atmospheres, *Space Sci. Rev.*, 16, 527–610, 1974.

Hansen, J., M. Sato, A. Lacis, and R. Ruedy, The missing climate forcing, *Philos. Trans. R. Soc. London, Ser. B*, 352, 231–240, 1997.

Hartigan, J. A., and M. A. Wong, Algorithm AS 136: A K-means clustering algorithm, *Appl. Stat.*, 28, 100–108, 1979.

Haywood, J. M., V. Ramaswamy, and B. J. Soden, Tropospheric aerosol climate forcing in clear-sky satellite observations over the oceans, *Science*, 283, 1299–1303, 1999.

Hegg, D., T. Larson, and P.-F. Yuen, A theoretical study of the effect of relative humidity on light scattering by tropospheric aerosols, *J. Geophys. Res.*, 98, 18,435–18,439, 1993.

Herman, J. R., P. K. Bhartia, O. Torres, C. Hsu, C. Seftor, and E. Celarier, Global distribution of UV-absorbing aerosols from Nimbus 7/TOMS data, *J. Geophys. Res.*, 102, 16,911–16,922, 1997.

Higurashi, A., and T. Nakajima, Development of a two-channel aerosol retrieval alogrithm on a global scale using NOAA AVHRR, *J. Atmos. Sci.*, 56, 924–941, 1999.

Husar, R. B., J. M. Prospero, and L. L. Stowe, Characterization of tropospheric aerosols over ocean with the NOAA-advanced very high resolution radiometer optical thickness operational product, *J. Geophys. Res.*, 102, 16,889–16,909, 1997.

Kahn, R., R. West, D. McDonald, B. Rheingans, and M. I. Mishchenko, Sensitivity of multiangle remote sensing observations to aerosol sphericity, *J. Geophys. Res.*, 102, 16,861–16,870, 1997.

Kahn, R., P. Banerjee, D. McDonald, and D. Diner, Sensitivity of multiangle imaging to aerosol optical depth, and to pure-particle size distribution and composition over ocean, *J. Geophys. Res.*, 103, 32,195–32,213, 1998.

Kahn, R., P. Banerjee, D. McDonald, and J. V. Martouchik, Aerosol properties derived from aircraft multiangle imaging over Monterey Bay, *J. Geophys. Res.*, in press, 2000.

Kopke, P., M. Hess, I. Schult, and E. Shettle, Global aerosol data set, *Max Planck Inst. Meteorol. Rep.*, 243, Hamburg, Germany, 1997.

Li, Z., L. Moreau, and A. Arking, On solar energy disposition: A perspective from observation and modeling, *Bull. Am. Meteorol. Soc.*, 78, 53–70, 1997.

Liousse, C., J. Penner, C. Chuang, J. Walton, H. Eddleman, and H. Cachier, A global three-dimensional model study of carbonaceous aerosols, *J. Geophys. Res.*, 101, 19,411–19,432, 1996.

Martonchik, J. V., D. J. Diner, R. Kahn, M. M. Verstraete, B. Pinty, H. R. Gordon, and T. P. Ackerman, Techniques for the retrieval of aerosol properties over land and ocean using multiangle imaging, *IEEE Trans. Geosci. Remote Sens.*, 36, 1212–1227, 1998.

Mishchenko, M. I., W. B. Rossow, A. Macke, and A. A. Lacis, Sensitivity of cirrus cloud albedo, bidirectional reflectance and optical thickness retrieval accuracy to ice particle shape, *J. Geophys. Res.*, 101, 16,973–16,985, 1996.

Mishchenko, M. I., L. Travis, R. Kahn, and R. West, Modeling phase functions for dust-like tropospheric aerosols using a shape mixture of randomly oriented polydisperse spheroids, *J. Geophys. Res.*, 102, 16,831–16,847, 1997.

Mishchenko, M. I., I. V. Geogdzhayev, B. Cairns, W. B. Rossow, and A. Lacis, Aerosol retrievals over the ocean by use of channels 1 and 2 AVHRR data: Sensitivity analysis and preliminary results, *Appl. Opt.*, 38, 7325–7341, 1999.

Nakajima, T., and A. Higurashi, A use of two-channel radiances for an aerosol characterization from space, *Geophys. Res. Lett.*, 25, 3815–3818, 1998.

Nakajima, T., A. Kigurashi, K. Aoki, T. Endoh, H. Fukushima, M. Toratani, Y. Mitomi, B. G. Mitechell, and R. Frouin, Earth phase analysis of OCTS radiance data for aerosol remote sensing, *IEEE Trans. Geosci. Remote Sens.*, 37, 1575–1585, 1999.

Penner, J. E., R. J. Charlson, J. M. Hales, N. S. Laulainen, R. Leifer, T. Novakov, J. Ogren, L. F. Radke, S. E. Schwartz, and L. Travis, Quantifying and minimizing uncertainty of climate forcing by anthropogenic aerosols, *Bull. Am. Meteorol. Soc.*, 75, 375–400, 1994.

Prospero, J. M., R. J. Charlson, V. Mohnen, R. Jaenicke, A. C. Delany, J. Moyers, W. Zoller, and K. Rahn, The atmospheric aerosol system: An overview, *Rev. Geophys. Space Phys.*, 21, 1607–1629, 1983.

Rao, C. R. N., L. L. Stowe, and E. P. McClain, Remote sensing of aerosols over the oceans using AVHRR data: Theory, practice and applications, *Int. J. Remote Sens.*, 10, 743–749, 1989.

Reid, J. S., P. V. Hobbs, R. J. Ferek, D. R. Blake, J. V. Martins, M. R. Dunlap, and C. Liousse, Physical, chemical, and optical properties of regional hazes dominated by smoke in Brazil, *J. Geophys. Res.*, 103, 32,059–32,080, 1998.

Shettle, E. P., and R. W. Fenn, Models for the aerosols of the lower atmosphere and the effects of humidity variations on their optical properties, *AFGL-TR-79-0214*, 94 pp., Air Force Geophys. Lab., Bedford, Mass., 1979.

Sokolik, I. N., and O. B. Toon, Direct radiative forcing by anthropogenic airborne mineral aerosols, *Nature*, 381, 681–683, 1996.

Stowe, L. L., A. M. Ignatov, and R. R. Singh, Development, validation, and potential enchancements to the second-generation operational aerosol product at the National Environmental Satellite, Data, and Information Service of the National Oceanic and Atmospheric Administration, *J. Geophys. Res.*, 102, 16,923–16,934, 1997.

Tanre, D., Y. J. Kaufman, M. Herman, and S. Mattoo, Remote sensing of aerosols over oceans using the MODIS/EOS spectral radiances, *J. Geophys. Res.*, 102, 16,971–16,988, 1997.

Tegen, I., and I. Fung, Contribution to the atmospheric mineral aerosol load from land surface modification, *J. Geophys. Res.*, 100, 18,707–18,726, 1995.

Tegen, I., P. Hollrig, M. Chin, I. Fung, D. Jacob, and J. Penner, Contribution of different aerosol species to the global aerosol extinction optical thickness: Estimates from model results, *J. Geophys. Res.*, 102, 23,895–23,915, 1997.

World Climate Programme (WCP), A preliminary cloudless standard atmosphere for radiation computation, *WCP-112*, 53 pp., Int. Assoc. for Meteorol. and Atmos. Phys., Boulder, CO, 1984.

P. Banerjee, R. Kahn, and D. McDonald, Jet Propulsion Laboratory, California Institute of Technology, MS 169-237, 4800 Oak Grove Drive, Pasadena CA 91109. (ralph.kahn@jpl.nasa.gov)